



**HAL**  
open science

## Cohesive GTN model for ductile fracture simulation

Noé Brice Nkoumbou Kaptchouang, Yann Monerie, Pierre-Guy Vincent,  
Frédéric Perales

► **To cite this version:**

Noé Brice Nkoumbou Kaptchouang, Yann Monerie, Pierre-Guy Vincent, Frédéric Perales. Cohesive GTN model for ductile fracture simulation. *Engineering Fracture Mechanics*, 2021, 242, pp.107437. 10.1016/j.engfracmech.2020.107437 . hal-03143810

**HAL Id: hal-03143810**

**<https://hal.science/hal-03143810v1>**

Submitted on 23 Feb 2021

**HAL** is a multi-disciplinary open access archive for the deposit and dissemination of scientific research documents, whether they are published or not. The documents may come from teaching and research institutions in France or abroad, or from public or private research centers.

L'archive ouverte pluridisciplinaire **HAL**, est destinée au dépôt et à la diffusion de documents scientifiques de niveau recherche, publiés ou non, émanant des établissements d'enseignement et de recherche français ou étrangers, des laboratoires publics ou privés.



Distributed under a Creative Commons Attribution - NonCommercial - NoDerivatives 4.0  
International License

# Cohesive GTN model for ductile fracture simulation

Noé Brice Nkoumbou Kaptchouang<sup>a,b</sup>, Yann Monerie<sup>b,c,\*</sup>, Pierre-Guy Vincent<sup>a,b</sup>, Frédéric Perales<sup>a,b</sup>

<sup>a</sup>*Institut de Radioprotection et de Sûreté Nucléaire, B.P. 3, 13115 Saint-Paul-lez-Durance Cedex, France*

<sup>b</sup>*MIST Laboratory, IRSN-CNRS-UM, B.P. 3, 13115 Saint-Paul-lez-Durance Cedex, France*

<sup>c</sup>*LMGC, Univ Montpellier, CNRS, Montpellier, France*

---

## Abstract

The present work addresses the micromechanical modeling and the simulation of crack initiation and propagation in ductile materials failing by void nucleation, growth and coalescence. A cohesive-volumetric approach is used and the overall material behavior is characterized both by a hardening bulk constitutive law and a softening surface traction-separation law embedded between each mesh of a finite element discretization. The traction-separation law sums up across a surface all the ductile damage processes occurring in a narrow strain localization band, while the bulk behavior concerns the other elasto-plastic effects. The proposed cohesive zone model is based on a micromechanical approach where the Gurson-Tvergaard-Needleman ductile damage model is adapted to the reduced kinematics of a surface while ensuring the complete effect of the strain rate or stress triaxiality both on the local plasticity and on the void growth. The corresponding cohesive model is implemented in the XPER computer code using the Non-Smooth Contact Dynamics method where cohesive models are introduced as mixed boundary conditions between each volumetric finite element. The present approach is applied to the simulation of crack growth in a standard ferritic steel. Results are compared with available experimental data. The efficiency of the proposed cohesive-GTN model is underlined since the shape of the cohesive law and its mechanical parameters arise directly from the micromechanical approach without any *ad hoc* fitting parameter.

*Keywords:* Ductile fracture, Cohesive zone model, GTN model, Crack growth simulation, Triaxiality effects

---

1

---

\*Corresponding author

*Email address:* [yann.monerie@umontpellier.fr](mailto:yann.monerie@umontpellier.fr) (Yann Monerie)

## Nomenclature

$\Omega, \partial\Omega$	domain and its boundary
$\dot{\mathbf{E}}$	strain rate
$\dot{E}_m, \dot{E}_{eq}$	hydrostatic and equivalent parts of the strain rate
$\eta_{\dot{\mathbf{E}}}$	strain rate triaxiality, equation (4)
$\dot{p}$	in-plane strain rate
$f$	porosity
$f^*$	effective porosity related to the void coalescence, equation (8)
$f_c$	porosity at onset of void coalescence
$f_f$	porosity at final failure
$\sigma_0$	yield stress of the matrix material surrounding the voids
$\sigma_y$	flow strength of the matrix material
$\bar{\epsilon}$	average plastic strain of the matrix material
$\mathbf{R}, [\mathbf{u}]$	stress vector and displacement jump across the cohesive zone
$\mathbf{n}, \mathbf{t}, \mathbf{s}$	vectors defining the normal-tangent basis
$h$	thickness of the localization band summarized by the cohesive zone
$H, D$	functions of Gurson model, equation (2)
$\chi$	couple of variables $\{\eta_{\dot{\mathbf{E}}}, q_1 f^*(f)\}$

## 1. Introduction

Many materials used in nuclear plants are polycrystalline materials that exhibit a ductile behavior at high temperature, e.g. ceramic materials such as uranium dioxide [1] or mixed oxide fuels, metallic alloys used for the reactor pressure vessels [2], structural components within the vessels, etc. Simulation of the fracture of these materials under accident conditions is of great interest when assessing the safety of nuclear plants. One of the process of ductile fracture is the nucleation and growth of microscopic voids under accumulation of plastic strain in some regions [3, 4]. As a consequence, these regions are softened and the deformations can localize into some narrow band, referred as *fracture process zone*, where coalescence of voids occurs and leads to main cracks [5].

On one hand, a widely used framework to describe such a damage process in ductile materials is the continuum micromechanics, based on a physical modeling of the kinematics of voids nucleation, growth and coalescence inside a matrix material. Within this approach, the Gurson-Tvergaard-Needleman (GTN) model [6–9] is surely the most widespread model to characterize the ductile fracture.

On the other hand, Cohesive Zone Models (CZM) are widely used as numerical models leading to creation of surface as a limit case of strain localization, [10, 11] among others. This phenomenological approach of fracture is based on the pioneering works of [12] and [13] who proposed to introduce a process zone at the crack tip in order to avoid the unrealistic unbounded stresses predicted by Linear Elastic Fracture Mechanics. In such an approach, the stress remains finite and tends to vanish while the crack tip is opening. In the standard cohesive surface theory of fracture, the crack growth is modeled as a decohesion of two surfaces within a continuum material. Therefore, the cohesive stress corresponds to the amount of stress which is needed to initiate the separation of the two surfaces. In this framework, the overall material behavior is characterized by two constitutive relations, the volumetric (bulk) stress–strain constitutive law and the traction–separation law across the cohesive surface embedded in a three-dimensional continuum. The traction–separation law is expressed as a relationship  $\mathbf{R} = \mathcal{R}([\mathbf{u}])$  between the stress vector  $\mathbf{R}$  and the displacement jump  $[\mathbf{u}]$  across the two surfaces. For a given material, the shape of the curve  $\mathcal{R}([\mathbf{u}])$  is generally unknown and many *a priori* shape functions are proposed in the literature, see [14–17] to cite few. The CZM is thus fully determined by the data of some mechanical surface parameters as cohesive energy and toughness [16, 18, 19].

It is worth noting that the particular case of the simulation of tearing of ductile metal plates with the help of

cohesive zone models has recently given rise to several papers [20–23]. As pointed out by [23], cohesive zone modeling is often combined in practical situations with shell modeling. Cohesive zone models have been elaborated and calibrated in these works, using numerical simulations and sometimes experimental results. In [21], a plate tearing problem is simulated and the measured overall force–displacement response is used to calibrate the cohesive zone. In [20], the complex sequence of events that occurs during failure is studied in details with a GTN model. During a mode I loading crack growth, the fracture process is simulated by a 2D plane strain finite element model. Then, the traction–separation relationship of the cohesive zone is determined. This work was extended in [23] by expanding the model to 3D.

The parameters of any CZM corresponding to a bulk ductile damage model don’t have to be considered as pure material parameters since the ductile failure based on void initiation, growth and coalescence is strongly dependent on the local stress and strain states [9, 24, 25]. Previous works have introduced *ad hoc* dependence of cohesive parameters on surrounding plastic state. For example, [26, 27] propose to add a dependence on the accumulated plastic strain of the material adjacent to the cohesive zone. In [28, 29], a stress triaxiality dependent cohesive model is formulated by the use of elastic-plastic constitutive relations combined with a softening law under plane strain and plane stress conditions. The behavior of the traction separation law up to the peak stress is established to replicate the linear elastic and strain hardening behavior of an undamaged material in plane strain [30] and plane stress [29]. The resulting behavior is therefore a function of the path in the stress space (thus the stress triaxiality) and elastic-plastic constants. The softening after the peak stress is characterized by an exponential smoothing function. Another approach to determine the ductile cohesive parameters from a micromechanical basis consists in considering a Representative Volume Element (RVE) composed of a Gurson-like material and identifying the cohesive parameters of an *a priori* given CZM to fit the overall response of the RVE. This idea has been introduced by [16] who studied the behavior of a GTN unit cell under uniaxial strain conditions. Since the void growth and coalescence at high stress triaxiality is the main microscopic mechanism of ductile fracture, this approach has been extended by [30–32] to take into account the local stress triaxiality as an internal variable of a cohesive model. They have determined the cohesive parameters dependence on the stress triaxiality by the numerical study of a plane strain or axisymmetric unit cell under different biaxial stress loadings. This approach has been further developed by [33, 34] for the case of rate-dependent GTN-type model.

Following the idea that the traction–separation law should represent the failure behavior of a unit material cell, the present work proposes to derive a CZM for ductile materials from a micromechanical approach. The objective is to obtain a CZM whose the shape as well as the parameters directly derive from a bulk ductile damage model, namely here the GTN model. The present paper is organized as follows. The second section details the modeling and the derivation of the CZM. The third section is devoted to its numerical implementation in the XPER computer code. In a fourth section, the simulation of crack growth in a standard ferritic steel shows the relevance of the approach by comparison to available experimental data.

## 2. Cohesive zone model for ductile failure

### 2.1. GTN model

Let us recall that Gurson yield surface [6] is based on the analysis of a hollow sphere (domain  $\Omega$ , porosity  $f$ ) made of a homogeneous and incompressible plastic matrix obeying to a von Mises yield criterion (J2 plasticity, yield stress  $\sigma_0$ ) and subjected to a homogeneous macroscopic strain rate  $\dot{\mathbf{E}}$  on its outer boundary  $\partial\Omega$ ,  $\mathbf{v} = \dot{\mathbf{E}} \cdot \mathbf{x}$  on  $\partial\Omega$ , where  $\mathbf{v}$  is the velocity field and  $\mathbf{x}$  is the position vector. The effective dissipation potential corresponding to Gurson yield surface reads [6, 35]:

$$\Phi^G(\dot{\mathbf{E}}) = \sigma_0 \int_f^1 \sqrt{\frac{4(\dot{E}_m)^2}{y^2} + (\dot{E}_{eq})^2} dy \quad (1)$$

where  $\dot{E}_m$  and  $\dot{E}_{eq}$  are respectively the hydrostatic and equivalent strain rates,  $\dot{E}_m = (1/3) \text{tr} \dot{\mathbf{E}}$ ,  $\dot{E}_{eq} = \sqrt{(2/3) \dot{\mathbf{E}}^d : \dot{\mathbf{E}}^d}$ ,  $\dot{\mathbf{E}}^d = \dot{\mathbf{E}} - \dot{E}_m \mathbf{i}$  denotes the deviatoric part of the effective strain rate, and  $\mathbf{i}$  is the second-

76 order identity tensor. A general expression of the integral (1) can be found in [35]:

$$\Phi^G(\dot{\mathbf{E}}) = \sigma_0 \dot{E}_{\text{eq}} [3\eta_{\dot{\mathbf{E}}} H(\eta_{\dot{\mathbf{E}}}, f) + D(\eta_{\dot{\mathbf{E}}}, f)] \quad (2)$$

77 with

$$H(\eta_{\dot{\mathbf{E}}}, f) = \frac{2}{3} \left( \operatorname{arcsinh} \left( \frac{2\eta_{\dot{\mathbf{E}}}}{f} \right) - \operatorname{arcsinh} (2\eta_{\dot{\mathbf{E}}}) \right) \quad \text{and} \quad D(\eta_{\dot{\mathbf{E}}}, f) = \sqrt{(2\eta_{\dot{\mathbf{E}}})^2 + 1} - \sqrt{(2\eta_{\dot{\mathbf{E}}})^2 + f^2} \quad (3)$$

78 where the effective strain rate triaxiality reads

$$\eta_{\dot{\mathbf{E}}} = \frac{\dot{E}_{\text{m}}}{\dot{E}_{\text{eq}}} \quad (4)$$

79 The macroscopic stress  $\Sigma = \partial\Phi^G/\partial\dot{\mathbf{E}}$  is derived from the effective potential (2)

$$\Sigma_{\text{m}} = \sigma_0 H(\eta_{\dot{\mathbf{E}}}, f) \quad \text{and} \quad \Sigma_{\text{eq}} = \sigma_0 D(\eta_{\dot{\mathbf{E}}}, f) \quad (5)$$

80 where  $\Sigma_{\text{m}} = (1/3)\operatorname{tr}\Sigma$  is the hydrostatic stress,  $\Sigma_{\text{eq}} = \sqrt{(3/2)\Sigma^{\text{d}} : \Sigma^{\text{d}}}$  the equivalent stress and  $\Sigma^{\text{d}} =$   
81  $\Sigma - \Sigma_{\text{m}} \mathbf{i}$  the deviatoric part of  $\Sigma$ . Gurson yield criterion is thus obtained by eliminating the kinematic  
82 parameter  $\eta_{\dot{\mathbf{E}}}$  between the hydrostatic and equivalent stresses in (5):

$$\phi^G(\Sigma, f) = \frac{\Sigma_{\text{eq}}^2}{\sigma_0^2} + 2f \cosh \left( \frac{3}{2} \frac{\Sigma_{\text{m}}}{\sigma_0} \right) - 1 - f^2 = 0 \quad (6)$$

83 Various modifications of the Gurson criterion have been progressively introduced in the literature to better fit  
84 unit-cell simulations or to take into account cavities interaction and coalescence, etc and can be summarized  
85 by the so-called Gurson-Tvergaard-Needleman (GTN) model [8]:

$$\phi^{\text{GTN}}(\Sigma, f) = \frac{\Sigma_{\text{eq}}^2}{\sigma_0^2} + 2q_1 f^* \cosh \left( \frac{3}{2} q_2 \frac{\Sigma_{\text{m}}}{\sigma_0} \right) - 1 - q_3 f^{*2} = 0 \quad (7)$$

86 where  $q_1, q_2, q_3 = q_1^2$  are constants and  $f^*$  is an effective porosity related to the void coalescence:

$$f^* = \begin{cases} f & \text{for } 0 \leq f \leq f_c \\ f_c + \frac{f_u^* - f_c}{f_f - f_c} (f - f_c) & \text{for } f_c \leq f \end{cases} \quad (8)$$

87 where  $f_c$  is the porosity at onset of void coalescence,  $f_f$  is the fracture porosity,  $f^*(f_f) = f_u^* = 1/q_1$ . The  
88 following notation is introduced  $k = (f_u^* - f_c)/(f_f - f_c)$ . Isotropic hardening can be introduced by replacing  
89  $\sigma_0$  with  $\sigma_y(\bar{\epsilon})$  in equation (7), where  $\sigma_y$  is the flow strength of the material surrounding the void. The  
90 scalar variable  $\bar{\epsilon}$  is interpreted as an 'average' plastic strain of the matrix material surrounding the void. Its  
91 evolution is governed by an equivalent plastic work expression:

$$\Sigma : \dot{\mathbf{E}} = (1 - f) \sigma_y \dot{\bar{\epsilon}} \quad (9)$$

92 The evolution of the void volume fraction is given by

$$\dot{f} = \dot{f}_g + \dot{f}_n \quad (10)$$

93 where  $\dot{f}_g$  is the void growth rate, derived from the conservation of mass

$$\dot{f}_g = (1 - f) \operatorname{tr} \dot{\mathbf{E}} \quad (11)$$

94 and where  $\dot{f}_n$  is the rate of void nucleation. In case of strain controlled nucleation, [36] suggest to approximate  
95 the nucleation of new cavities by a normal distribution

$$\dot{f}_n = A \dot{\bar{\epsilon}} \quad \text{where} \quad A(\bar{\epsilon}) = \frac{f_N}{s_N \sqrt{2\pi}} \exp \left( -\frac{1}{2} \left( \frac{\bar{\epsilon} - \epsilon_N}{s_N} \right)^2 \right) \quad (12)$$

96 where  $f_N$  is the volume fraction of void nucleating particles,  $\epsilon_N$  is an average nucleation strain parameter  
97 and  $s_N$  is a standard deviation. By doing so, the rate of void nucleation depends on the 'average' plastic  
98 strain  $\bar{\epsilon}$  and its time derivative.

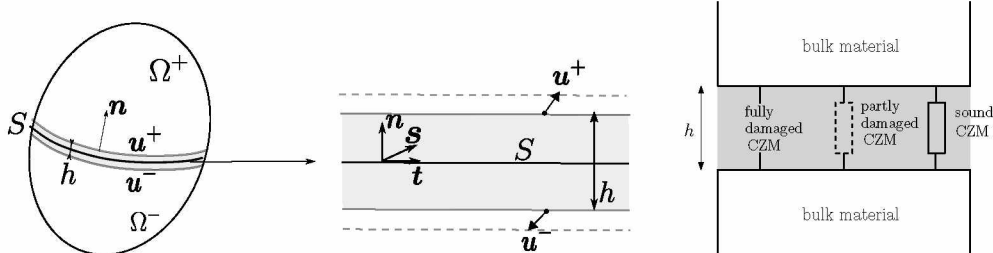


Figure 1: Displacement jump across a localization band of thickness  $h$ . The ductile damage process is summarized inside this band with the help of a surface cohesive zone model having the same behavior as a bulk GTN model. The damage intensity corresponds to the effective porosity given in (8).

## 2.2. Cohesive interface model

Let us consider that the material domain  $\Omega$  is made of an elastic plastic material composed of two regions,  $\Omega^-$  and  $\Omega^+$ , separated by a strain localization band (unit normal vector  $\mathbf{n}$ ), Figure 1. Outside the localization band, the material follows a J2 plasticity model without damage. Ductile damage occurs only inside the strain localization band and its behavior is described by the GTN model (7). The *thickness*  $h$  of the localization band is small compared to a characteristic length of  $\Omega$ . This narrow band is then modeled as a cohesive surface  $S$  between  $\Omega^-$  and  $\Omega^+$  as usually done in problems of adhesive solids [37, 38]. Designating by  $\mathbf{u}^+$  and  $\mathbf{u}^-$  the respective values of the displacement fields at the boundaries of  $\Omega^+$  and  $\Omega^-$  shared with  $S$ , the displacement jump across  $S$  is defined as:

$$[\mathbf{u}] = \mathbf{u}^+ - \mathbf{u}^- = [u_n]\mathbf{n} + [u_t]\mathbf{t} + [u_s]\mathbf{s} \quad (13)$$

in the local basis  $(\mathbf{n}, \mathbf{t}, \mathbf{s})$  where  $\mathbf{t}$  and  $\mathbf{s}$  are two unit vectors defining the tangent plane. Following [37, 39, 40], the strain rate on the cohesive surface can be approximated with the help of a scaling rule:

$$\dot{\mathbf{E}} \approx \frac{[\dot{\mathbf{u}}] \otimes_s \mathbf{n}}{h} = \frac{[\dot{u}_i]n_j + [\dot{u}_j]n_i}{2h} = \begin{bmatrix} \frac{[\dot{u}_n]}{h} & \frac{[\dot{u}_t]}{2h} & \frac{[\dot{u}_s]}{2h} \\ \frac{[\dot{u}_t]}{2h} & 0 & 0 \\ \frac{[\dot{u}_s]}{2h} & 0 & 0 \end{bmatrix} \quad (14)$$

All these softening effects occurring into the localization band are here summarized into a zero thickness cohesive surface. In the present work, the parameter  $h$  is thus more related to the thickness of the localization band than to the void spacing length as previously proposed in [28, 31, 32, 41, 42].

In such an approximation, the in-plane components of the strain rate are neglected. The hydrostatic part and the equivalent part of the strain rate read respectively

$$\dot{E}_m = \frac{1}{3} \frac{[\dot{u}_n]}{h}, \quad \dot{E}_{eq} = \frac{2}{3} \sqrt{\left(\frac{[\dot{u}_n]}{h}\right)^2 + \frac{3}{4} \frac{[\dot{u}_t]^2}{h^2} + \frac{3}{4} \frac{[\dot{u}_s]^2}{h^2}}$$

The strain rate triaxiality is thus obtained as

$$\eta_{\dot{\mathbf{E}}} = \frac{[\dot{u}_n]}{2\sqrt{[\dot{u}_n]^2 + \frac{3}{4}[\dot{u}_t]^2 + \frac{3}{4}[\dot{u}_s]^2}}$$

The strain rate triaxiality  $\eta_{\dot{\mathbf{E}}}$  is bounded by above by 1/2, limiting the void growth rate in equation (11). This is a strong limitation to develop surface cohesive model for ductile damage. This limitation is directly linked to the reduced kinematics of a surface. To overcome this limitation, two strategies can be considered. First, information about the current loading state can be transferred from the volumetric domains  $\Omega^+$  and

117  $\Omega^-$  to the cohesive zone  $S$ . The underlying hypothesis is that the loading state inside the cohesive band  
 118 remains close to the nearest continuum elements adjacent to the cohesive band. This idea was introduced  
 119 by [27], who proposed a cohesive law depending on the average of the accumulated plastic strain over a bulk  
 120 finite element adjacent to the cohesive zone. This idea was further extended by [31] who introduced the  
 121 cohesive parameters dependence on the stress triaxiality of a continuum element adjacent to the cohesive  
 122 zone. In the latter, the evolution of cohesive parameters with respect to the stress triaxiality was identified  
 123 by simulating the behavior of a plane strain element obeying to a GTN model under different biaxial load-  
 124 ings.

125 Second, the dependence of cohesive models on the stress-strain state can be improved by incorporating  
 126 additional in-plane terms in the cohesive strain rate (14). [43] propose to determine these in-plane terms  
 127 through the values at each side of the cohesive zone (so from the nearest volumetric elements) to enforce a  
 128 continuity of the strain. In the present work, in order to enhance the range of stress and strain states afford-  
 129 able by the cohesive model, it is proposed to extend the cohesive kinematics by introducing an additional  
 130 in-plane strain rate  $\dot{p}$ :

$$\dot{\mathbf{E}} \approx \frac{[\dot{\mathbf{u}}] \otimes_s \mathbf{n}}{h} + \dot{p} (\mathbf{t} \otimes_s \mathbf{t} + \mathbf{s} \otimes_s \mathbf{s}) = \begin{bmatrix} \frac{[\dot{u}_n]}{h} & \frac{[\dot{u}_t]}{2h} & \frac{[\dot{u}_s]}{2h} \\ \frac{[\dot{u}_t]}{2h} & \dot{p} & 0 \\ \frac{[\dot{u}_s]}{2h} & 0 & \dot{p} \end{bmatrix} \quad (15)$$

131 This simple choice allows the strain-rate triaxiality  $\eta_{\dot{\mathbf{E}}}$  to range within  $]-\infty, +\infty[$ . The rate  $\dot{p}$  depends on  
 132 the loading state provided by the volumetric finite element adjacent to the cohesive zone as presented in  
 133 section 3.

### 134 2.3. Traction-separation law

135 Since the local behavior on  $S$  is described by the GTN plasticity model, the surface stress vector is  
 136 related to the strain rate

$$\mathbf{R} = \boldsymbol{\Sigma} \cdot \mathbf{n} = \left( \Sigma_m \mathbf{i} + \frac{2}{3} \frac{\Sigma_{\text{eq}}}{\dot{E}_{\text{eq}}} \dot{\mathbf{E}}^d \right) \cdot \mathbf{n} \quad (16)$$

137 with  $\Sigma_m$  and  $\Sigma_{\text{eq}}$  given by (5). A normalized stress tensor  $\bar{\boldsymbol{\Sigma}}$  is then defined and the stress vector  $\mathbf{R}$ , or  
 138 cohesive stress, reads

$$\bar{\boldsymbol{\Sigma}} = \frac{1}{\sigma_y} \boldsymbol{\Sigma} \quad \text{thus} \quad \mathbf{R} = \sigma_y \bar{\boldsymbol{\Sigma}} \cdot \mathbf{n} \quad \text{where} \quad \bar{\boldsymbol{\Sigma}} \cdot \mathbf{n} = \begin{cases} \bar{\Sigma}_{nn} = \frac{1}{q_2} H(\chi) + \frac{4}{9} D(\chi) \frac{1}{\dot{E}_{\text{eq}}} \left( \frac{[\dot{u}_n]}{h} - \dot{p} \right) \\ \bar{\Sigma}_{nt} = \frac{1}{3} D(\chi) \frac{1}{\dot{E}_{\text{eq}}} \frac{[\dot{u}_t]}{h} \\ \bar{\Sigma}_{ns} = \frac{1}{3} D(\chi) \frac{1}{\dot{E}_{\text{eq}}} \frac{[\dot{u}_s]}{h} \end{cases} \quad (17)$$

139 and

$$\dot{E}_{\text{eq}} = \frac{2}{3} \sqrt{\left( \frac{[\dot{u}_n]}{h} - \dot{p} \right)^2 + \frac{3}{4} \frac{[\dot{u}_t]^2}{h^2} + \frac{3}{4} \frac{[\dot{u}_s]^2}{h^2}}, \quad \eta_{\dot{\mathbf{E}}} = \frac{\frac{[\dot{u}_n]}{h} + 2\dot{p}}{2\sqrt{\left( \frac{[\dot{u}_n]}{h} - \dot{p} \right)^2 + \frac{3}{4} \frac{[\dot{u}_t]^2}{h^2} + \frac{3}{4} \frac{[\dot{u}_s]^2}{h^2}}} \quad (18)$$

140 where  $\chi$  stands for the couple of variables  $\chi = \{\eta_{\dot{\mathbf{E}}}, q_1 f^*(f)\}$ . Equation (17) shows that this cohesive  
 141 formulation can be used in 3D since the stress vector is fully described and under mixed mode conditions  
 142 since all components of the displacement jump have an independent role. The effect of the strain-rate  
 143 triaxiality is taken into account through the variable  $\chi$  in functions  $H$  and  $D$ .

144 The effective porosity  $f^*$  is expressed in terms of porosity  $f$  with (8). The evolution law of porosity (10)  
 145 (including nucleation) reads

$$\dot{f} = (1 - f) \left( \frac{[\dot{u}_n]}{h} + 2\dot{p} \right) + A\dot{\bar{\varepsilon}} \quad (19)$$

146 and hardening is estimated through the average plastic strain  $\bar{\varepsilon}$  using (9)

$$\dot{\bar{\varepsilon}} = \frac{1}{1 - f} \left( \bar{\Sigma}_{nn} \frac{[\dot{u}_n]}{h} + \bar{\Sigma}_{nt} \frac{[\dot{u}_t]}{h} + \bar{\Sigma}_{ns} \frac{[\dot{u}_s]}{h} + (\bar{\Sigma}_{tt} + \bar{\Sigma}_{ss}) \dot{p} \right) \quad (20)$$

$$\bar{\Sigma}_{tt} = \bar{\Sigma}_{ss} = \frac{1}{q_2} H(\chi) - \frac{2}{9} D(\chi) \frac{1}{E_{\text{eq}}} \left( \frac{[\dot{u}_n]}{h} - \dot{p} \right) \quad (21)$$

148 It is worth noting that the evolution law of  $\bar{\varepsilon}$  is independent of the hardening law  $\sigma_y(\bar{\varepsilon})$ . Moreover we  
 149 underline that this GTN traction-separation law can simulate ductile fracture as soon as the porosity rate  $\dot{f}$   
 150 is not vanishing. In other words, there is no need for macroscopic crack like defect to initiate and propagate  
 151 a ductile crack with this model. We chose in the sequel to illustrate the ability of the model a compact  
 152 tension specimen but other situations can be treated as for example notched tensile bars.

#### 153 2.4. Time integration of the constitutive equations

154 For sake of simplicity, the dependence in time is omitted for the current time  $t$ , and thus  $\mathbf{E}$ ,  $f$  and  $\bar{\varepsilon}$   
 155 denote respectively the strain, the porosity and the average plastic strain at time  $t$ . Their values at the  
 156 previous time step  $t - \delta t$  are denoted by a superscript  $(t - \delta t)$ ,  $\mathbf{E}^{(t - \delta t)}$ ,  $f^{(t - \delta t)}$  and  $\bar{\varepsilon}^{(t - \delta t)}$ . The strain  
 157 increment  $\delta \mathbf{E} = \mathbf{E} - \mathbf{E}^{(t - \delta t)}$  is introduced. Using an explicit scheme, the time discretized equations thus  
 158 read

$$f = f^{(t - \delta t)} + (1 - f^{(t - \delta t)}) (\delta E_{nn} + 2\delta p) + A(\bar{\varepsilon}^{(t - \delta t)}) \delta \bar{\varepsilon} \quad (22)$$

$$\bar{\varepsilon} = \bar{\varepsilon}^{(t - \delta t)} + \delta \bar{\varepsilon} \quad \text{with} \quad \delta \bar{\varepsilon} = \frac{\bar{\Sigma}_{nn} \delta E_{nn} + 2\bar{\Sigma}_{nt} \delta E_{nt} + 2\bar{\Sigma}_{ns} \delta E_{ns} + \bar{\Sigma}_{tt} \delta p + \bar{\Sigma}_{ss} \delta p}{1 - f^{(t - \delta t)}} \quad (23)$$

160 and

$$\left\{ \begin{array}{l} \bar{\Sigma}_{nn} = \frac{1}{q_2} H(\chi^{(t - \delta t)}) + \frac{4}{9} D(\chi^{(t - \delta t)}) \frac{\delta E_{nn} - \delta p}{(\delta \mathbf{E})_{\text{eq}}} \\ \bar{\Sigma}_{nt} = \frac{2}{3} D(\chi^{(t - \delta t)}) \frac{\delta E_{nt}}{(\delta \mathbf{E})_{\text{eq}}} \\ \bar{\Sigma}_{ns} = \frac{2}{3} D(\chi^{(t - \delta t)}) \frac{\delta E_{ns}}{(\delta \mathbf{E})_{\text{eq}}} \\ \bar{\Sigma}_{tt} = \bar{\Sigma}_{ss} = \frac{1}{q_2} H(\chi^{(t - \delta t)}) - \frac{2}{9} D(\chi^{(t - \delta t)}) \frac{\delta E_{nn} - \delta p}{(\delta \mathbf{E})_{\text{eq}}} \\ \eta_{\mathbf{E}} = \frac{(\delta \mathbf{E})_{\text{m}}}{(\delta \mathbf{E})_{\text{eq}}} \end{array} \right. \quad (24)$$

161 where  $\chi^{(t - \delta t)}$  stands now for  $\{\eta_{\mathbf{E}}, q_1 f^*(f^{(t - \delta t)})\}$ . Thus, knowing the strain tensor at time  $t$ , together with  
 162 the strain, porosity and average strain at time  $t - \delta t$ , the porosity and the average strain are updated using  
 163 equations (22), (23) and (24). Then components of the cohesive stress are evaluated straightforwardly at  
 164 time  $t$

$$\left\{ \begin{array}{l} R_n = \sigma_y(\bar{\varepsilon}) \left( \frac{1}{q_2} H(\chi) + \frac{4}{9} D(\chi) \frac{\delta E_{nn} - \delta p}{(\delta \mathbf{E})_{\text{eq}}} \right) \\ R_t = \sigma_y(\bar{\varepsilon}) \frac{2}{3} D(\chi) \frac{\delta E_{nt}}{(\delta \mathbf{E})_{\text{eq}}} \\ R_s = \sigma_y(\bar{\varepsilon}) \frac{2}{3} D(\chi) \frac{\delta E_{ns}}{(\delta \mathbf{E})_{\text{eq}}} \end{array} \right. \quad (25)$$



165 *2.5. Traction–separation behavior under various loadings*

166 In order to illustrate the potentialities of the corresponding GTN traction–separation law, we use a  
 167 Swift-like model to describe the hardening of the material

$$\sigma_y(\bar{\epsilon}) = \sigma_0(1 + K\bar{\epsilon})^{1/n} \quad (26)$$

168 where the yield stress  $\sigma_0$  and the constants  $K$  and  $n$  are set to fit the experimental plastic flow data given  
 169 by [32]. The material parameters of the study are specified in Table 1, where  $Y$  denotes the Young modulus  
 170 and  $\nu$  the Poisson ratio.

Elasticity	$Y$	$\nu$						
	210 GPa	0.3						
Hardening	$\sigma_0$	$K$	$n$					
	470 MPa	35.0	4.5					
GTN	$q_1$	$q_2$	$f_0$	$k$	$f_c$	$f_N$	$\epsilon_N$	$s_N$
	1.5	1.0	0.0025	3.4	0.021	0.02	0.3	0.1

Table 1: Material parameters for a ferritic steel StE460 (German designation) from [32].

171

172

First, let us consider a constant axisymmetric strain rate with the following strain

$$\mathbf{E} = \begin{bmatrix} \dot{E}_{nn} & 0 & 0 \\ 0 & r \dot{E}_{nn} & 0 \\ 0 & 0 & r \dot{E}_{nn} \end{bmatrix} \times t \quad \text{and} \quad \frac{1}{2} \leq r < 1, \dot{E}_{nn} > 0 \text{ kept constant} \quad (27)$$

The strain-rate triaxiality reads

$$\eta_{\dot{\mathbf{E}}} = \frac{1 + 2r}{2(1 - r)}$$

173 Note that since the loading is proportional, the strain-rate triaxiality corresponds exactly to the strain  
 174 triaxiality  $\eta_{\mathbf{E}} = E_m/E_{eq}$ . Prescribing the value of  $r = -1/2, -1/3, 0, 1/2, 2/3$  corresponds to an imposed  
 175 strain triaxiality  $\eta_{\mathbf{E}} = 0, 0.125, 0.5, 2, 3.5$ . The evolution of the normal cohesive stress  $R_n/\sigma_0$  (or  $\Sigma_{nn}/\sigma_0$ )  
 176 with respect to the normal opening  $[u_n]/h$  (or equivalently with respect to the strain component  $E_{nn}$ )  
 177 is plotted in Figure 2 (left) for the cohesive model and for a GTN material point under various strain  
 178 triaxialities. The response of the GTN material point has been evaluated using the implicit algorithm of  
 179 [44] dedicated to a class of pressure-dependent plasticity models.

180 These curves represent the cohesive traction–separation response corresponding to a unit cell made of a  
 181 GTN material with a Swift hardening model. Since no elasticity is incorporated in the cohesive model at  
 182 this stage, the corresponding traction–separation law is *extrinsic*, by opposition to *intrinsic* models where  
 183 the cohesive response has an initial slope. Contrarily, the GTN material point response presents an initial  
 184 slope because elasticity has been taken into account in the resolution of the GTN model. This explains the  
 185 slight difference between the cohesive model and the GTN material point responses particularly highlighted  
 186 for  $\eta_{\mathbf{E}} = 0.125$  in Figure 2. Here, in the cohesive model, no crack tip opening is observed as long as the  
 187 cohesive stress does not reach a given threshold. When the strain triaxiality is vanishing, this threshold is  
 188 lower than the yield stress of the underlying matrix  $\sigma_0$ . This threshold is about 3 – 4 times the yield stress  
 189 when the strain triaxiality is larger than 0.1. Roughly speaking, for non vanishing strain triaxiality, if a  
 190 ductile cohesive zone has a toughness  $R_0$ , the surface damage occurs when the remote loading reaches about  
 191  $R_0/3$  or  $R_0/4$ . This simple result is compatible with other numerical observations [45].  
 192 Moreover, when the damage occurs, the cohesive stress decreases rapidly with respect to the crack opening  
 193 and the ductile CZM is rather brittle for such non vanishing strain triaxiality. The cohesive ductility de-  
 194 creases when the strain triaxiality increases.

195

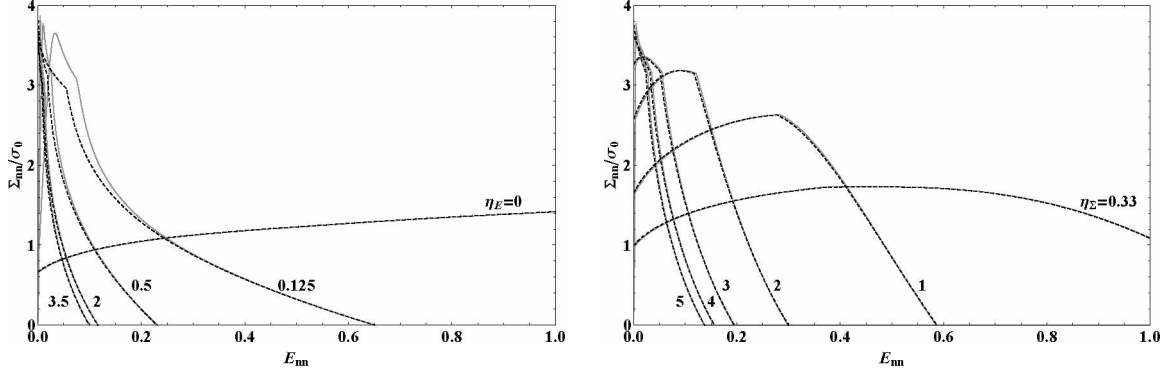


Figure 2: Response of the cohesive model (dashed line) and a GTN material point (solid line) for (left) various strain triaxialities (axisymmetric strain) and (right) various stress triaxialities (axisymmetric stress).

196 Second, let us consider a prescribed direction of axisymmetric stress:

$$\Sigma(t) = k(t) \Sigma^o = k(t) \begin{bmatrix} 1 & 0 & 0 \\ 0 & r^* & 0 \\ 0 & 0 & r^* \end{bmatrix} \quad \text{and} \quad \frac{1}{2} \leq r^* < 1 \text{ kept constant} \quad (28)$$

197 where  $\Sigma^o$  is a known tensor prescribing the direction of the stress,  $k(t)$  is an unknown scalar defining the  
 198 amplitude of the stress. The procedure of [46] is applied. It consists in finding  $\mathbf{E}(t)$  and  $k(t)$  from the  
 199 following set of equations:

$$\begin{cases} \Sigma(t) = k(t) \Sigma^o & \text{constitutive equations} \\ \Sigma^o : \mathbf{E}(t) = x \end{cases} \quad (29)$$

where  $x$  is a prescribed loading parameter. Here, a constant and positive value is prescribed for  $\hat{x}$  and the  
 evolution for the loading parameter is  $x = \hat{x} t$ . The stress triaxiality reads

$$\eta_{\Sigma} = \frac{\Sigma_m}{\Sigma_{\text{eq}}} = \frac{1 + 2r^*}{3(1 - r^*)}$$

200 Since the stress is imposed to be axisymmetric, the strain is also axisymmetric. Moreover, the stress  
 201 triaxiality  $\eta_{\Sigma}$  is prescribed. At the beginning of each time step, the value of  $E_{nn}$  is increased and the  
 202 increment  $\delta E_{nn}$  reads  $E_{nn} - E_{nn}^{(t-\delta t)}$ . The increment of  $p$  (or  $E_{tt}$ ), denoted by  $\delta p$ , is searched such that:

$$\eta_{\Sigma} = \frac{1}{q_2} \frac{H(\eta_{\delta \mathbf{E}}, q_1 f^*(f^{(t-\delta t)}))}{D(\eta_{\delta \mathbf{E}}, q_1 f^*(f^{(t-\delta t)}))} \quad \text{with} \quad \eta_{\delta \mathbf{E}} = \frac{(\delta \mathbf{E})_m}{(\delta \mathbf{E})_{\text{eq}}} \quad (30)$$

203 Equation (30) is solved by using a Newton-Raphson algorithm, leading to an updated value for  $\eta_{\delta \mathbf{E}}$ . The  
 204 value of  $\delta p$  can thus be calculated by relationships presented in Appendix A, leading to an updated value  
 205 for  $p$ . This is performed at the beginning of each time step of the explicit integration scheme presented in  
 206 subsection 2.4. The evolution of  $R_n/\sigma_0$  as a function of  $E_{nn}$  (or  $[u_n]/h$ ) from the cohesive model is plotted  
 207 in Figure 2 (right) for various stress triaxialities. Again, the corresponding cohesive response is *extrinsic*  
 208 and the cohesive ductility decreases when the strain triaxiality increases, but the cohesive model appears  
 209 more ductile for this type of loadings. The peak stress is higher than the initial cohesive thershold and  
 210 corresponds to the critical porosity  $f_c$ .

211 For both type of loadings, Figure 2 illustrates the high impact of the stress and strain triaxialities on the  
 212 evolution of the normal cohesive stress. The cohesive strength and the cohesive energy (area under the curve)  
 213 are strongly dependent on the strain and stress triaxialities, Figure 3. The greater the strain triaxiality,  
 214 the brittle the cohesive zone: the strength increases with respect to the strain triaxiality while the cohesive  
 215 energy decreases. Same type of results were already pointed out by [31] and as expected, damage is hard to

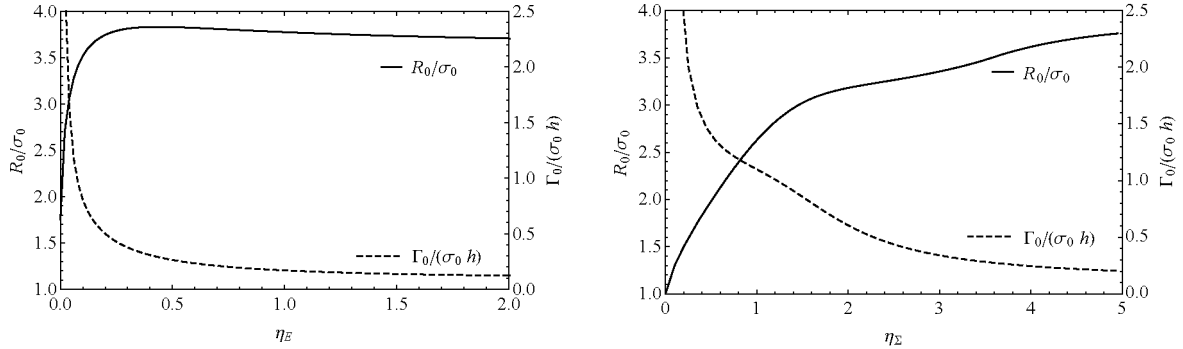


Figure 3: Dependence of the cohesive strength (left axis, black line) and of the cohesive energy (right axis, dashed line) on the strain triaxiality  $\eta_E$  (Left) or on the stress triaxiality  $\eta_\Sigma$  (Right).

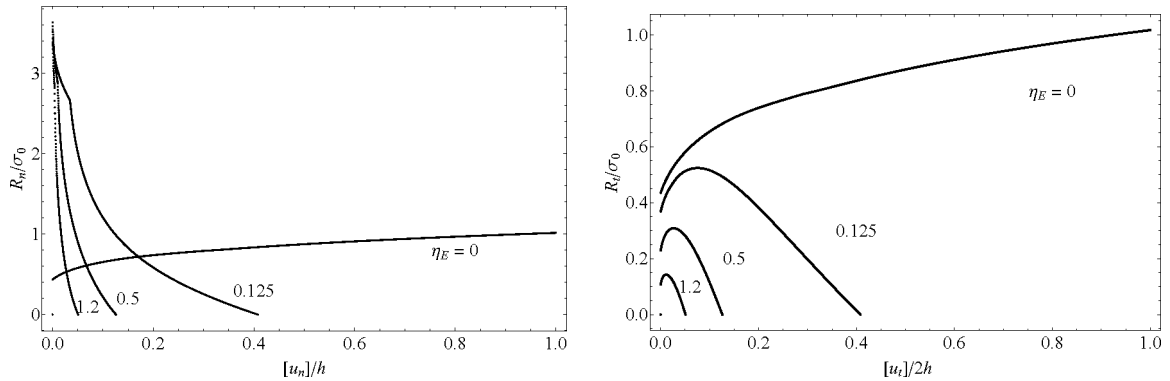


Figure 4: Response of the cohesive model under a mixed mode loading (31) for various strain triaxialities.

216 develop at very low triaxiality. The maximal normal stress that the cohesive zone can tolerate is reached for  
 217 a strain triaxiality about 1/2. This lack of damage for low triaxiality loadings is a limitation of the original  
 218 Gurson model. Nevertheless, note that the model can predict damage for intermediate triaxiality loadings  
 219 with shear. To illustrate this point, let us consider the following loading combining a normal separation  $[u_n]$   
 220 and a tangential separation  $[u_t]$  (with  $E_{nn} = [u_n]/h$  and  $E_{nt} = [u_t]/(2h)$ ):

$$\mathbf{E} = \begin{bmatrix} \dot{E} & \dot{E} & 0 \\ \dot{E} & r\dot{E} & 0 \\ 0 & 0 & r\dot{E} \end{bmatrix} \times t \quad \text{with } \dot{E} > 0 \text{ kept constant} \quad (31)$$

221 Prescribing the value of  $r = -0.5, -0.23, 0.4, 1.8$  corresponds to an imposed strain triaxiality  $\eta_E \approx$   
 222  $0, 0.125, 0.5, 1.2$ . The evolution of  $R_n/\sigma_0$  (or  $R_t/\sigma_0$ ) as a function of  $[u_n]/h$  (or  $[u_t]/(2h)$ ) from the cohesive  
 223 model is plotted in Figure 4. Imposing a tangential separation leads to a non-zero tangential stress vector  
 224 which exhibits damage for intermediate triaxialities.

225 Again, note that there is no fitting parameter in the obtained cohesive model. Once the GTN parameters  
 226 are known, the cohesive model is fully defined. This is a major feature of the proposed cohesive model.

### 227 3. Numerical implementation into a cohesive-volumetric finite element formulation

228 The numerical simulations are performed using the XPER software dedicated to the simulation of frac-  
 229 ture dynamics of heterogeneous materials [47, 48]. This computer code proposes a periodic homogenization  
 230 framework under small or finite strain theories, but it can also be used for more general structure computa-  
 231 tions. XPER implementation involves a multi-contact modeling strategy based on the Non-Smooth Contact

232 Dynamics (NSCD) method where cohesive models are introduced as mixed boundary conditions between  
 233 each volumetric finite element. Each element or either a group of elements of the mesh can be considered as  
 234 an independent body and the interface between bodies follows a frictional CZM with no regularization nor  
 235 penalization. CZM are introduced by a slight modification of Signorini-Coulomb conditions [45, 49]. The  
 236 bulk behavior inside each element corresponds to a hardening behavior without any damage. The damage  
 237 is modeled at the interface between bodies by the cohesive law. Moreover, the NSCD method avoids insta-  
 238 bilities arising with softening models, see [45, 50] for details.

239 For the numerical implementation, one has first to specify how the variable  $\dot{p}$  is updated during the com-  
 240 putation. Then, some changes have been performed regarding the cohesive zone model. Indeed, as XPER  
 241 typically uses *intrinsic* cohesive zone models, a modification of the cohesive model is proposed hereafter  
 242 to change it from extrinsic to intrinsic. Furthermore, as in a fully general structure computation the load-  
 243 ing may be followed by an unloading situation, it has to be introduced in the cohesive model. Thus, the  
 244 cohesive model is enriched to ensure that the unloading case is properly handled. Finally, the model has  
 245 been implemented under the assumption of proportional loading and the cohesive stress given by (25) is  
 246 estimated using the total cohesive strain  $\mathbf{E}$  instead of the strain increment tensor  $\delta\mathbf{E}$ . As in the deformation  
 247 theory, this approach is valid under the restrictive case of a monotonous and proportional loading, but from  
 248 numerical standpoint allows a simpler numerical integration of the cohesive model.

### 249 3.1. Estimate of the in-plane strain rate $\dot{p}$

250 The strain rate  $\dot{p}$  is estimated by considering information coming from the volumetric elements adjacent  
 251 to the cohesive zone. Among several possibilities, it is chosen here to compute  $\dot{p}$  by maintaining the equality  
 252 between the strain-rate triaxiality  $\eta_{\mathbf{E}}$  in the cohesive zone and the strain-rate triaxiality  $\eta_{\mathbf{E}}^{\text{vol}}$  computed from  
 253 the stress state in a volumetric element adjacent to the cohesive zone. From the normality rule, GTN model  
 254 leads to:

$$255 \quad \dot{\mathbf{E}} = \dot{\lambda} \left( \frac{q_1 q_2 f^*}{\sigma_y} \sinh \left( \frac{3}{2} q_2 \frac{\Sigma_m}{\sigma_y} \right) \mathbf{i} + \frac{3}{\sigma_y^2} \Sigma^d \right) \quad \text{with} \quad \dot{\lambda} > 0 \quad (32)$$

256 Substituting in this expression the average stress tensor over the volumetric slave element (denoted by  $\Sigma^{\text{vol}}$ )  
 adjacent to the cohesive zone, the corresponding strain rate triaxiality reads

$$257 \quad \eta_{\mathbf{E}}^{\text{vol}} = \frac{q_1 q_2 f^* \sinh \left( \frac{3}{2} q_2 \frac{\Sigma_m^{\text{vol}}}{\sigma_y} \right)}{2 \frac{\Sigma_{\text{eq}}^{\text{vol}}}{\sigma_y}} \quad (33)$$

From (15), the strain-rate triaxiality in the cohesive zone reads:

$$258 \quad \eta_{\mathbf{E}} = \frac{\frac{[\dot{u}_n]}{h} + 2\dot{p}}{2 \sqrt{\left( \frac{[\dot{u}_n]}{h} - \dot{p} \right)^2 + \frac{3}{4} \frac{[\dot{u}_t]^2}{h^2} + \frac{3}{4} \frac{[\dot{u}_s]^2}{h^2}}} \quad (34)$$

259 By equating (33) and (34) the strain rate  $\dot{p}$  is determined. It appears that  $\dot{p}$  evolves as a function of the  
 260 cohesive kinematics and the stress state of the adjacent volumetric slave element. Only the case  $[\dot{u}_n] > 0$ ,  
 261 corresponding to a positive loading, is considered here (the unloading case  $[\dot{u}_n] < 0$  will be separately treated  
 262 in section 3.3) and different expressions for  $\dot{p}$  are determined (see Appendix A for a detailed description).  
 The selected expressions are reported in Table 2.

263 From the C(T) test simulations presented in section 4, it was observed that the resulting triaxiality  
 264  $\eta_{\mathbf{E}}^{\text{vol}}$  decreases when increasing the damage in the cohesive zone. Since the model does not predict any  
 265 damage for low triaxiality, the rupture is artificially delayed. To address this issue, the volumetric stress  
 266  $\Sigma^{\text{vol}}$  is transferred to the cohesive zone up to the onset of coalescence (when  $f$  reaches  $f_c$ ). Over the void  
 267 coalescence, the value of  $\Sigma^{\text{vol}}$  is kept constant during the post-coalescence stage and the stress triaxiality  
 268 does not evolve anymore, see Figure 9 in the sequel.

$\eta_{\mathbf{E}}^{\text{vol}}$	$\dot{p}([\dot{\mathbf{u}}], \eta_{\mathbf{E}}^{\text{vol}})$
$\eta_{\mathbf{E}}^{\text{vol}} < 0$	$\dot{p} = -\frac{[\dot{u}_n]}{2h}$
$0 \leq \eta_{\mathbf{E}}^{\text{vol}} < 1$ and $\eta_{\mathbf{E}}^{\text{vol}} > 1$	$\dot{p} = \frac{2(\eta_{\mathbf{E}}^{\text{vol}})^2 + 1}{2((\eta_{\mathbf{E}}^{\text{vol}})^2 - 1)} \frac{[\dot{u}_n]}{h} - \frac{ \eta_{\mathbf{E}}^{\text{vol}}  \sqrt{9\frac{[\dot{u}_n]^2}{h^2} + 3(1 - (\eta_{\mathbf{E}}^{\text{vol}})^2) \left(\frac{[\dot{u}_t]^2}{h^2} + \frac{[\dot{u}_s]^2}{h^2}\right)}}{2((\eta_{\mathbf{E}}^{\text{vol}})^2 - 1)}$
$\eta_{\mathbf{E}}^{\text{vol}} = 1$	$\dot{p} = \frac{1}{4} \frac{[\dot{u}_n]^2 + [\dot{u}_t]^2 + [\dot{u}_s]^2}{[\dot{u}_n]h}$

Table 2: Expressions of in-plane strain rate components  $\dot{p}$  depending on crack tip opening rate  $[\dot{\mathbf{u}}]$  and surrounding volumetric strain rate triaxiality  $\eta_{\mathbf{E}}^{\text{vol}}$ .

### 3.2. Intrinsic cohesive zone model

We propose here a simple manner to convert an extrinsic CZM to an intrinsic one. The stress vector  $\mathbf{R}$  is multiplied by a positive increasing function that rapidly tends to 1 with respect to the crack opening. The resulting stress vector is denoted by  $\mathbf{R}^{(\text{int})}$ :

$$\mathbf{R}^{(\text{int})} = \begin{cases} R_n^{(\text{int})} = \left(1 - \exp\left(-\alpha_n \frac{[u_n]}{h}\right)\right) \times R_n \\ R_t^{(\text{int})} = \left(1 - \exp\left(-\alpha_t \frac{|[u_t]|}{h}\right)\right) \times R_t \\ R_s^{(\text{int})} = \left(1 - \exp\left(-\alpha_s \frac{|[u_s]|}{h}\right)\right) \times R_s \end{cases} \quad (35)$$

The initial stiffness is calibrated through the parameters  $\alpha_n$ ,  $\alpha_t$ , and  $\alpha_s$  that have been calculated with the help of equations (B.4), (B.8) and (B.9) given in Appendix B.

### 3.3. Unloading case

Since local unloading can occur during a crack growth in a fully general structure computation, one need to specify the behavior of the cohesive zone model during unloading taking into account the irreversibility of the damage process.

A criterion has to be defined to distinguish loading state and unloading state. It is chosen to handle the unloading in each direction separately. It means that an unloading can occur in one direction while the other directions are still loaded. In the normal direction, unloading occurs if:

$$[u_n]^{(t)} - [u_n]^{(t-\delta t)} < 0 \quad (36)$$

For the tangential directions, unloading occurs respectively in  $\mathbf{t}$  or  $\mathbf{s}$  directions if:

$$|[u_t]^{(t)}| - |[u_t]^{(t-\delta t)}| < 0 \quad \text{or} \quad |[u_s]^{(t)}| - |[u_s]^{(t-\delta t)}| < 0 \quad (37)$$

One has also to define the behavior of the cohesive zone during unloading. The maximum values of separation in each direction that have occurred during the loading process are introduced to take into account the loading history in the cohesive zone and the irreversibility of the damage process

$$[u_i]_{\max} = \max_{0 \leq \tau \leq t} |[u_i](\tau)| \quad \text{with } i = n, t, s \quad (38)$$

Following [51], the unloading behavior is assumed to be an elastic unloading up to the origin and a further elastic reloading also:

$$\bar{\mathbf{R}} = \left(R_n^{(\text{int})}\right)_{\max} \frac{[u_n]}{[u_n]_{\max}} \mathbf{n} + \left(R_t^{(\text{int})}\right)_{\max} \frac{[u_t]}{[u_t]_{\max}} \mathbf{t} + \left(R_s^{(\text{int})}\right)_{\max} \frac{[u_s]}{[u_s]_{\max}} \mathbf{s} \quad (39)$$

288 where the  $(R_i^{(int)})_{\max}$  are the components of the cohesive stress  $\mathbf{R}^{(int)}$  evaluated at the maximal opening  
 289  $[u_i]_{\max}$ ,  $i = n, t, s$ . The unloading rule described in (39) is illustrated in Figure 5. For sake of simplicity, the  
 290 stress vector  $\bar{\mathbf{R}}$  is simply denoted by  $\mathbf{R}$  in Figure 5 and in the next section. The unloading behavior is then  
 291 completed by assuming the irreversibility of the damage and the hardening during the loading process:

$$\forall \tau \in [0, t], \quad \dot{f}(\tau) \geq 0 \quad \text{and} \quad \dot{\bar{\varepsilon}}(\tau) \geq 0 \quad (40)$$

292 From a practical point of view, two additional tests are performed in the integration scheme to meet the  
 293 conditions (40):

$$\text{if } f < f^{(t-\delta t)} \quad \text{then } f = f^{(t-\delta t)} \quad \text{and} \quad \text{if } \bar{\varepsilon} < \bar{\varepsilon}^{(t-\delta t)} \quad \text{then } \bar{\varepsilon} = \bar{\varepsilon}^{(t-\delta t)} \quad (41)$$

294 The general equations of the cohesive zone model are summarized in Appendix C. It is worth noting that  
 295 this elastic unloading is not really realistic. During an unloading voids closure can occur involving some  
 296 compressive plastic effects. This effect is not taken into account here but a simple elastic unloading allows  
 to avoid spurious effects when unloading of CZM arises.

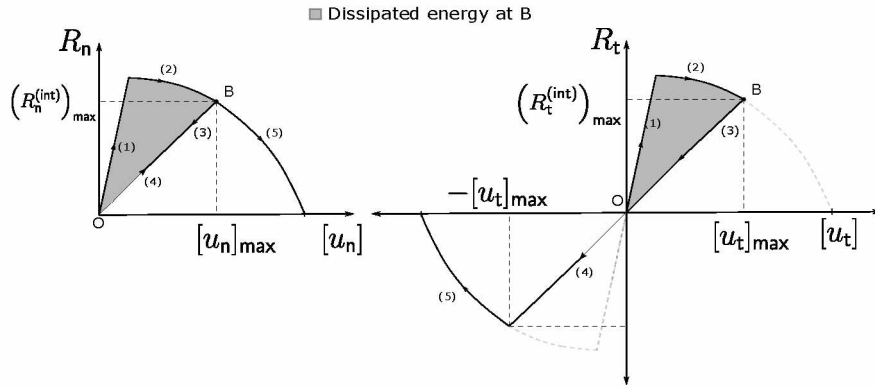


Figure 5: Illustration of the unloading rule. (1) initial loading, (2) loading (softening), (3) unloading, (4) reloading, (5) loading (softening). (a) normal direction, (b) tangential direction.

297

#### 298 4. Application: simulation of compact tensile tests

299 The cohesive zone model is applied to simulate crack growth in a compact tension C(T) specimen under  
 300 the plane strain conditions. The objective here is to illustrate the ability of the new cohesive zone model to  
 301 simulate crack growth. Full 3D simulations are left for future work. The material under consideration is a  
 302 ferritic steel StE460 (German designation) for which experimental data of crack growth tests and parameters  
 303 for the GTN model have already been reported in many works [30, 32, 52, 53]. The material parameters are  
 304 reported in Table 1. The material surrounding the cohesive zones is an elastic-plastic solid with hardening  
 305 law (26), identical to the matrix surrounding the voids in the GTN analysis.

306 A material length scale of  $\Lambda = 200 \mu m$  has been used with these material properties in [32, 53], as a typical  
 307 value for the ductile fracture in ferritic steels. In these papers, the numerical simulations are performed on  
 308 one half of the specimen making use of the symmetry boundary conditions. The cohesive properties (energy  
 309  $\Gamma_0$  and strength  $R_0$ ) used to model the half of the process zone were calibrated on a single element of size  
 310  $\Lambda \times \Lambda$  with the GTN model representing a unit cell of material. Thus, the total cohesive energy per crack  
 311 increment is  $2\Gamma_0$ . Here, the numerical simulations are performed on a full specimen and since the dissipated  
 312 energy in a single element is proportional to the size of the element, the parameter  $h$  is chosen as the size  
 313 of a square cell of area  $2\Lambda^2$ , with  $h = \sqrt{2} \times 200 \mu m$ , here overestimated by  $h \approx 300 \mu m$ . The  $C_n$  and  $C_t$   
 314 parameters are set to  $10^{18} Pa/m$  in order to respect the criterion  $C_n = C_t > 21Y/l_{\text{mesh}}$  theoretically derived

$l_{\text{mesh}}$	number of elements in the central zone	total number of elements
200 $\mu\text{m}$	1600	20220
150 $\mu\text{m}$	2809	26198
100 $\mu\text{m}$	6400	38020
50 $\mu\text{m}$	25000	112638

Table 3: Mesh size and number of elements

315 by [54] even for the smallest mesh size used in this paper  $l_{\text{mesh}} \approx 50 \mu\text{m}$ .  
316 The dimensions of the standard C(T) side-grooved specimen used for the tests are:  $W = 50 \text{ mm}$  (width),  
317  $a_0/W = 0.59$  (initial relative crack length),  $B = 25 \text{ mm}$  (thickness),  $B_n = 19 \text{ mm}$  (net thickness between  
318 side grooves). The experimental so-called  $R$ -Curve in terms of  $J - \Delta a$  from these tests are reported in  
319 [30, 32, 52, 53].

320 The simulations are performed with two-dimensional 4 nodes linear plane strain  $Q1$  elements and two contact  
321 nodes per cohesive zones are introduced (no significant interpenetration even in case of local rotation). The  
322 specimen is located in the  $x$ - $y$  plane. The finite element mesh is depicted on Figure 6. Since the crack path  
323 is known, cohesive zones are only put along the line in front of the crack tip, assuming pure mode I crack  
324 propagation. The model thus contains a series of cohesive elements located along a line in front of the crack  
325 tip which is taken to be initially sharp. The mesh is refined in front of the crack tip, over an initial surface  
326  $8 \text{ mm} \times 8 \text{ mm}$ , and the bulk elements in this central zone have the initial dimension  $l_{\text{mesh}} \times l_{\text{mesh}}$ . A coarser  
327 mesh is used out of this zone. Information concerning the mesh are specified in Table 3. The two circular  
328 holes are partially filled with a purely elastic material (same Young modulus and Poisson ratio as specified  
329 in Table 1) in order to apply the loading without any bias on the local shear stress. The loading consists in  
330 imposing the vertical component along the  $y$  axis of the velocity to  $\dot{U}_y$  for the upper part of the specimen  
331 and to  $-\dot{U}_y$  for the lower part of the specimen. The calculation are made using an explicit finite element  
332 solver with an implicit contact resolution, see [48] for details. Since softening behaviors induce instabilities,  
333 a dynamical formulation is here employed, again see [48]. This formulation however requires very small  
334 time steps ( $\delta t$  about  $10^{-9} \text{ s}$  to  $10^{-8} \text{ s}$ ). Since instantaneous behavior laws are invoked, a high velocity is  
335 prescribed ( $\dot{U}_y = 0.1 \text{ m.s}^{-1}$ ) in order to counterbalance the small time step and run the simulations in a  
reasonable time. The mass density of the material is set to  $7.8 \times 10^3 \text{ kg/m}^3$ .

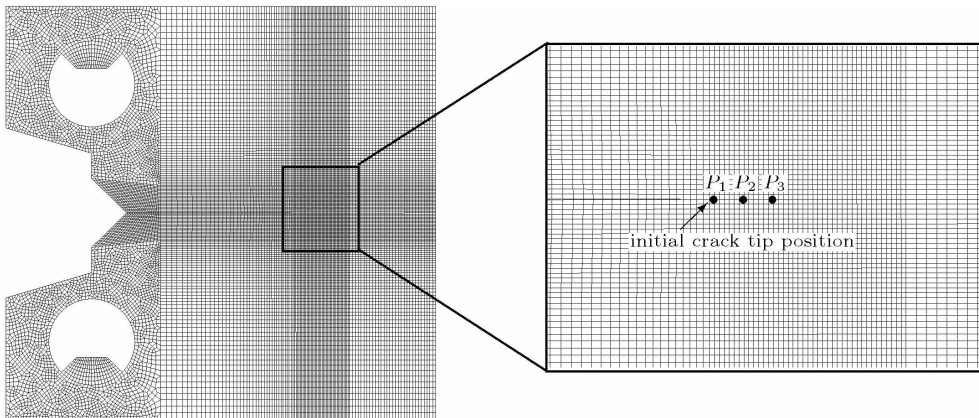


Figure 6: C(T) specimen mesh with mesh size at the crack tip  $l_{\text{mesh}} = 200 \mu\text{m}$ . Three positions ahead of the crack tip:  $P_1$  at initial crack tip,  $P_2$  one millimeter ahead,  $P_3$  two millimeter ahead.

336

#### 337 4.1. Results

338 The numerical overall response of the C(T) is compared in Figure 7 (left) to experimental data of [55].  
339 Since the simulations are computed in 2D under plane strain assumption and the specimen is side grooved,

340 the effective thickness  $B_{\text{eff}} = \sqrt{B \times B_n}$  is considered for the calculation of the resulting forces, see [55]. The  
 341 overall agreement is good since *there is no parameter to adjust*. The crack growth resistance curve is also  
 342 well predicted. The  $J$ -integral versus crack extension  $\Delta a$  is evaluated using ASTM E1820 formula [56] and  
 343 compared to experimental data of [30] in Figure 7 (right). The numerical model is found to be in reasonable  
 accordance with the experiments.

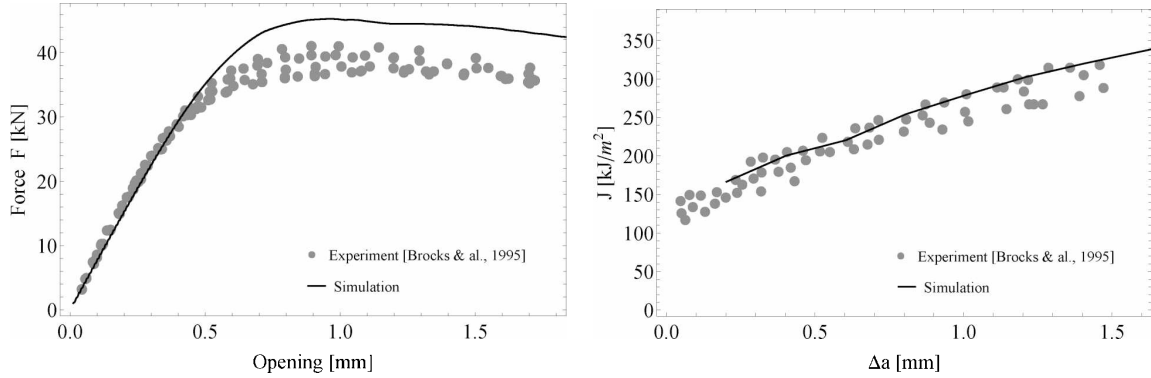


Figure 7: Cohesive-Volumetric finite element simulation (thick lines) vs experiments (gray points). (Left) Overall response: Load  $F$  vs opening displacement  $v$ , experiments of [55]. (Right) Crack growth resistance curve:  $J$ -integral vs crack extension  $\Delta a$ , experiments of [55].

344 During the crack propagation, plasticity develops in the vicinity of the crack tip where tension occurs and  
 345 at the free boundary ahead of the crack tip where intense compressible loadings are supported, see Figure 8.  
 346 The von Mises stress field and the cumulated plastic strain field thus exhibit non trivial spatial structures  
 347 in the vicinity of the crack tip. The resulting stress and strain triaxiality fields also exhibit complex spatial  
 348 structure.

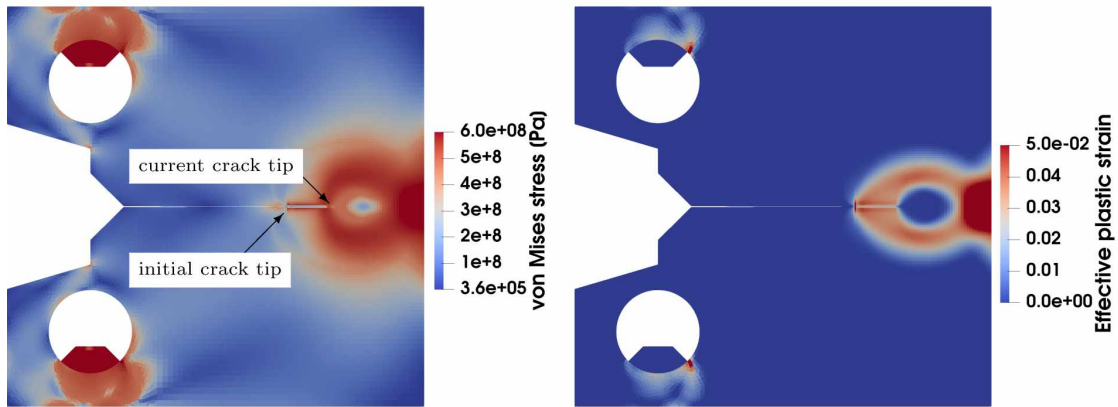


Figure 8: Equivalent von Mises stress field (left) and cumulated plastic strain field (right) at crack length  $\Delta a = 6 \text{ mm}$ .

349 As expected, the local CZM that drives the crack propagation depends on this spatial distribution of  
 350 the triaxiality fields and thus on the position ahead of the crack tip, Figure 9. Since the evolution of local  
 351 stress triaxiality with respect to the overall loading is not the same at point  $P_1$  where the crack propagation  
 352 initiates than at point  $P_2$  where the crack propagation reaches a steady state, the associated local cohesive  
 353 response is also not the same. Point  $P_3$  is in the same steady state as point  $P_2$ , its local response is the  
 354 same as  $P_2$  and thus not plotted on the figure. It is readily to see that more cohesive energy is needed to  
 355



356 initiate the crack propagation than to propagate it in a steady state. Note that the simulations of [21] for  
 357 analyzing the mode I crack advance initiating from a pre-crack in a large scale plate structure led to the  
 358 opposite trend. The plate was modeled with shell elements and nodal spring-type cohesive elements were  
 359 used along the crack path. They obtained a relatively small cohesive energy for elements immediately ahead  
 360 of the pre-crack tip. Thus the result obtained in the present paper must be dependent of the plane strain  
 361 conditions. A full study with a comparison between 2D plane strain, 2D plane stress and 3D simulations  
 362 would be required to discuss this point in depth. It is also worth noting that the shape of the local cohesive  
 363 response is not *a priori* given and arises from the loading and the micromechanical model. It is again a  
 364 significant feature of the model. At the crack onset, the CZM is rather a door-like model, while it looks like  
 a triangular one during crack propagation. The peak stress stays about 3 times of the yield stress.

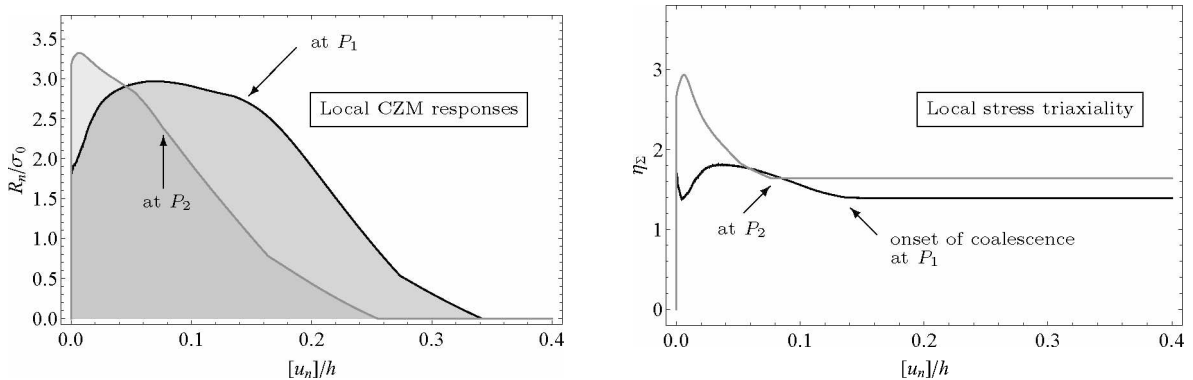


Figure 9: The local cohesive responses at point  $P_1$  (initial crack tip) and  $P_2$  (1 mm ahead of the crack tip) are different (left) since the local stress triaxiality  $\eta_{\Sigma}$  does not evolve as the same manner at these points during the macroscopic loading (right). The stress triaxiality is fixed to a constant value at the onset of coalescence.

365  
 366 Coherence of the results can be reinforced with the help of a simple estimate. Focusing on Figure 9 (b),  
 367 the stress triaxiality  $\eta_{\Sigma}$  at the crack tip and at the onset of coalescence is about  $\eta_{\Sigma} \simeq 1.4$ . For this stress  
 368 triaxiality value, results obtained in Figure 3 (b) give  $\Gamma_0/(\sigma_0 h) \simeq 0.9$ . Identifying the mode I cohesive  
 369 energy  $\Gamma_0$  to the critical value  $J_{Ic}$  of the  $J$ -integral and estimating  $J_{Ic} \simeq 145 \text{ kJ/m}^2$  in Figure 7 (b) for a  
 370 crack extension  $\Delta a \simeq 0.2 \text{ mm}$  (see [57]), one obtains  $h \simeq 340 \mu\text{m}$  which is fully consistent with the value  
 371 used in these calculations ( $h = 300 \mu\text{m}$ ).

#### 372 4.2. Length scale parameter and mesh size sensitivity

373 Figure 10 (left) exhibits the macroscopic response for different values of the length scale parameter  $h$ . As  
 374 expected, the overall response is strengthened when increasing  $h$  while keeping mesh size  $l_{\text{mesh}}$  constant. The  
 375 parameter  $h$  scales the local energy dissipated by the cohesive zones. When  $h$  increases it can be considered  
 376 that the cohesive energy is smeared out over a larger length and the effect of localization decreases.  
 377 Contrarily, the overall response is strengthened when decreasing  $l_{\text{mesh}}$  while keeping length scale parameter  
 378  $h$  constant, Figure 10 (right). This effect is more unusual since, in the local approach of continuum damage  
 379 mechanics, the dissipated energy vanishes when the element size tends to zero as a consequence of the  
 380 damage localization within a single band of elements [58]. Here, the cohesive energy is dissipated along the  
 381 cohesive zones and not in the bulk elements. A scale effect arises: when the mesh size  $l_{\text{mesh}}$  decreases, the  
 382  $h$ -length acts over a larger part of the surrounding finite elements and again, it can be considered that the  
 383 cohesive energy is smeared out over a larger length.

384 An artificial hardening is thus obtained when decreasing  $l_{\text{mesh}}$  while keeping mesh size  $h$  constant. This  
 385 hardening can be counterbalanced by adjusting the value of length scale parameter  $h$  with respect to the  
 386 mesh size  $l_{\text{mesh}}$ . Figure 11 shows that it is possible to get an overall load-opening response independent on  
 387 the mesh size if the length scale parameter is set conveniently. The linear fit  $h \simeq 220 + 0.4 l_{\text{mesh}}$  (in  $\mu\text{m}$ )  
 388 seems accurate for the current simulations.

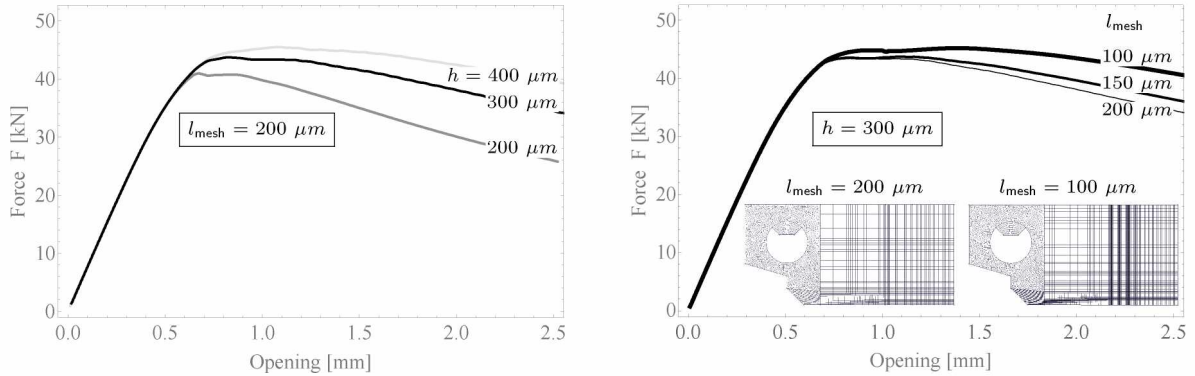


Figure 10: Cohesive-Volumetric finite element simulations, overall load-opening response. Dependence on the thickness parameter for mesh size  $l_{\text{mesh}} = 200 \mu\text{m}$  (Left) and dependence on the mesh size for thickness parameter  $h = 300 \mu\text{m}$  (Right). Inset: upper part of the corresponding meshes, with mesh refinement in the process zone.

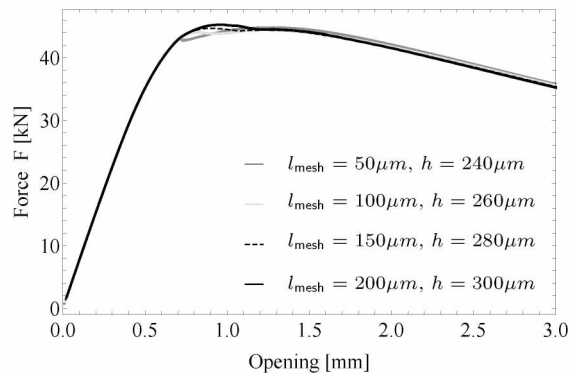


Figure 11: Adapting the length scale parameter  $h$  with respect to the mesh size  $l_{\text{mesh}}$  in order to obtain converged overall load-opening response.

## 389 5. Conclusion

390 In this paper the problem of simulating the crack initiation and growth in ductile materials failing  
391 by void nucleation, growth and coalescence is investigated. A crack surface is considered to be a limit  
392 case of strain localization band leading to a discontinuity of displacement field. The cohesive-volumetric  
393 approach appears to be a suitable framework for the description of discontinuity inside a material. In  
394 this framework, the hardening behavior of the material is described by the bulk behavior and the damage  
395 is described as a cohesive surface with a corresponding traction–separation law. Since in ductile fracture  
396 the material separation depends on the local stress and strain states which are strongly dependent on the  
397 geometry, a triaxiality-dependent cohesive model is derived. The cohesive surface is approximated as a band  
398 of small thickness whose behavior follows a volumetric GTN model. The obtained traction–separation law  
399 is a GTN-like model with reduced kinematics. This approach introduces a regularizing length parameter  $h$   
400 whose the link with the physical size of the localization band remains to be investigated. The GTN traction–  
401 separation law reproduces the behavior of a single volumetric element made of a GTN material. It accurately  
402 captures the stress or strain rate triaxiality dependence but suffers from the same limitation as the GTN  
403 model and does not predict any damage at low triaxiality. However the procedure developed is general and  
404 could be extended to more sophisticated micro-mechanical model which takes into account damage at low  
405 triaxiality or even viscoplastic effects. The application of this approach to simulate crack propagation in a  
406 standard compact tension specimen of ferritic steel shows the ability of the cohesive-volumetric approach  
407 to simulate crack growth in ductile material. The results are consistent with previous results obtained by

408 other authors. The application also exhibits the dependence of the regularization parameter  $h$  on a material  
 409 length characterizing the microstructure and the mesh size. The main result of this work is the ability to  
 410 derive CZM from any softening bulk behavior without any *a priori* assumptions on the shape of the cohesive  
 411 model. Many previous numerical constations are here re-obtained with no fitting parameters.

## 412 Appendix A. Expressions of $\dot{p}$

413 First, let us consider the case  $\eta_{\mathbf{E}}^{\text{vol}} \geq 0$  corresponding to tension. Condition  $\eta_{\mathbf{E}}^2 = \left(\eta_{\mathbf{E}}^{\text{vol}}\right)^2$  leads to the  
 414 following solutions for  $\dot{p}$ .

415 If  $\eta_{\mathbf{E}}^{\text{vol}} = 1$ , the solution is straightforward

$$\dot{p} = \frac{1}{4} \frac{[\dot{u}_{\mathbf{n}}]^2 + [\dot{u}_{\mathbf{t}}]^2 + [\dot{u}_{\mathbf{s}}]^2}{[\dot{u}_{\mathbf{n}}]h} \quad (\text{A.1})$$

416 If  $\eta_{\mathbf{E}}^{\text{vol}} \neq 1$ ,

$$\dot{p}_{\pm} = \frac{2\left(\eta_{\mathbf{E}}^{\text{vol}}\right)^2 + 1}{2\left(\left(\eta_{\mathbf{E}}^{\text{vol}}\right)^2 - 1\right)} \frac{[\dot{u}_{\mathbf{n}}]}{h} \pm \frac{\left|\eta_{\mathbf{E}}^{\text{vol}}\right| \sqrt{9\frac{[\dot{u}_{\mathbf{n}}]^2}{h^2} + 3\left(1 - \left(\eta_{\mathbf{E}}^{\text{vol}}\right)^2\right) \left(\frac{[\dot{u}_{\mathbf{t}}]^2}{h^2} + \frac{[\dot{u}_{\mathbf{s}}]^2}{h^2}\right)}}{2\left(\left(\eta_{\mathbf{E}}^{\text{vol}}\right)^2 - 1\right)} \quad (\text{A.2})$$

For  $0 \leq \eta_{\mathbf{E}}^{\text{vol}} < 1$ , it appears that the negative branch should be selected, using the inequalities:

$$\dot{p} \geq -[\dot{u}_{\mathbf{n}}]/(2h), \quad \frac{2\left(\eta_{\mathbf{E}}^{\text{vol}}\right)^2 + 1}{2\left(\left(\eta_{\mathbf{E}}^{\text{vol}}\right)^2 - 1\right)} \leq -1/2, \quad \left(\eta_{\mathbf{E}}^{\text{vol}}\right)^2 - 1 < 0$$

417 For  $\eta_{\mathbf{E}}^{\text{vol}} > 1$ , considering that the normal strain rate in the cohesive zone  $[\dot{u}_{\mathbf{n}}]/h$  should be greater than the  
 418 transverse strain rate  $\dot{p}$ , it appears from (A.2) that the negative branch should also be selected (using the  
 419 inequalities:  $[2\left(\eta_{\mathbf{E}}^{\text{vol}}\right)^2 + 1]/[2\left(\left(\eta_{\mathbf{E}}^{\text{vol}}\right)^2 - 1\right)] > 1$  and  $\left(\eta_{\mathbf{E}}^{\text{vol}}\right)^2 - 1 > 0$ ).

420 Secondly, let us consider the case  $\eta_{\mathbf{E}}^{\text{vol}} < 0$  corresponding to a compression state. The evolution law of the  
 421 porosity (19) indicates that the porosity is decreasing. Keeping in mind that the damage variable can only  
 422 be a growing function, it is chosen here to determine  $\dot{p}$  from the zero triaxiality  $\eta_{\mathbf{E}}^{\text{vol}} = 0$ . It leads to:

$$\dot{p} = -\frac{[\dot{u}_{\mathbf{n}}]}{2h} \quad (\text{A.3})$$

## 423 Appendix B. Expressions of $\alpha_{\mathbf{n}}$ , $\alpha_{\mathbf{t}}$ , and $\alpha_{\mathbf{s}}$

424 The initial slope of the function  $R^{(\text{int})}$  is typically denoted by  $C_{\mathbf{n}}$  in the normal direction and  $C_{\mathbf{t}} = C_{\mathbf{s}}$   
 425 in the tangential directions. It is known that the insertion of intrinsic cohesive models into finite element  
 426 meshes leads to an additional compliance in the overall force-displacement response. Therefore, the cohesive  
 427 stiffness has to be set high enough to avoid additional compliance in the material, but not too large in other  
 428 to avoid numerical instabilities. Various criteria are available to calibrate the cohesive stiffness for given  
 429 material properties and a given mesh [59–61]. Here, parameters  $\alpha_{\mathbf{n}}$ ,  $\alpha_{\mathbf{t}}$  and  $\alpha_{\mathbf{s}}$  are expressed in terms of  $C_{\mathbf{n}}$   
 430 and  $C_{\mathbf{t}}$ . By doing so, existing criteria derived for  $C_{\mathbf{n}}$  and  $C_{\mathbf{t}}$  can be directly used to adjust  $\alpha_{\mathbf{n}}$ ,  $\alpha_{\mathbf{t}}$  and  $\alpha_{\mathbf{s}}$ .  
 431 Let us consider a simple case of uniaxial tensile loading with no hardening ( $\sigma_y = \sigma_0$ ):

$$\mathbf{E} = \begin{bmatrix} \dot{E}_{\mathbf{nn}} & 0 & 0 \\ 0 & 0 & 0 \\ 0 & 0 & 0 \end{bmatrix} \times t, \quad \text{and } \dot{E}_{\mathbf{nn}} > 0 \text{ kept constant} \quad (\text{B.1})$$

432 In this case, the normal stress vector reads:

$$R_n^{(\text{int})} = \sigma_0 \left( \frac{1}{q_2} H\left(\frac{1}{2}, q_1 f^*\right) + \frac{2}{3} D\left(\frac{1}{2}, q_1 f^*\right) \right) \left( 1 - \exp\left(-\alpha_n \frac{[u_n]}{h}\right) \right) \quad (\text{B.2})$$

433 By imposing:

$$\frac{\partial R_n^{(\text{int})}}{\partial [u_n]} ([u_n] = 0) = C_n \quad (\text{B.3})$$

434 the parameter  $\alpha_n$  reads:

$$\alpha_n = \frac{C_n h}{\sigma_0 \left( \frac{1}{q_2} H\left(\frac{1}{2}, q_1 f^*(f_0)\right) + \frac{2}{3} D\left(\frac{1}{2}, q_1 f^*(f_0)\right) \right)} \quad (\text{B.4})$$

435 This expression is used in the numerical simulations (section 4) to estimate  $\alpha_n$ . A similar approach can be  
436 followed to estimate  $\alpha_t$ . Let us consider a simple case of pure shear loading with no hardening ( $\sigma_y = \sigma_0$ ):

$$\mathbf{E} = \begin{bmatrix} 0 & \dot{E}_{nt} & 0 \\ \dot{E}_{nt} & 0 & 0 \\ 0 & 0 & 0 \end{bmatrix} \times t \quad \text{and } \dot{E}_{tt} > 0 \text{ kept constant} \quad (\text{B.5})$$

437 In this case, the tangential stress vector reads:

$$R_t^{(\text{int})} = \sigma_0 \frac{1}{\sqrt{3}} (1 - q_1 f^*) \left( 1 - \exp\left(-\alpha_t \frac{[u_t]}{h}\right) \right) \quad (\text{B.6})$$

438 By imposing:

$$\frac{\partial R_t^{(\text{int})}}{\partial [u_t]} ([u_t] = 0) = C_t \quad (\text{B.7})$$

439 the parameter  $\alpha_t$  reads:

$$\alpha_t = \frac{\sqrt{3} C_t h}{\sigma_0 (1 - q_1 f^*(f_0))} \quad (\text{B.8})$$

440 This expression is used in the numerical simulations (section 4) to estimate  $\alpha_t$ . A similar expression can be  
441 obtained for  $\alpha_s$  from a  $C_s$  parameter:

$$\alpha_s = \frac{\sqrt{3} C_s h}{\sigma_0 (1 - q_1 f^*(f_0))} \quad (\text{B.9})$$

## 442 Appendix C. General equations of the cohesive zone model

443 The general equations used for the numerical implementation of the cohesive model are summarized  
444 below.

445 For each time  $t$ , the opening vector ( $[u_n]$ ,  $[u_t]$ ,  $[u_s]$ ) is known and the maximal values are updated:

$$[u_i]_{\max} = \max_{0 \leq \tau \leq t} |[u_i](\tau)| \quad \text{with } i = n, t, s \quad (\text{C.1})$$

The following quantities are computed from the maximal openings:

$$\epsilon_{nn} = \frac{[u_n]_{\max}}{h}, \quad \epsilon_{nt} = \frac{[u_t]_{\max}}{2h}, \quad \epsilon_{ns} = \frac{[u_s]_{\max}}{2h}$$

446 The previous values  $\epsilon_{nn}^{(t-\delta t)}$ ,  $\epsilon_{nt}^{(t-\delta t)}$ ,  $\epsilon_{ns}^{(t-\delta t)}$ , the porosity  $f^{(t-\delta t)}$  and the average strain  $\bar{\varepsilon}^{(t-\delta t)}$  are known.  
447 The differences between two time steps are denoted by a  $\delta$  (e.g.  $\delta\epsilon_{nn} = \epsilon_{nn} - \epsilon_{nn}^{(t-\delta t)}$ ). If  $f^{(t-\delta t)} < f_c$ , then  
448 the volumetric stress  $\Sigma^{\text{vol}}$  is updated. Otherwise it is maintained to the previous value.

449 The first step consists in updating the values of the porosity and the average strain from the following  
 450 equations.

$$\eta_E^{\text{vol}} = \frac{q_1 q_2 f^*(f^{(t-\delta t)}) \sinh\left(\frac{3}{2} q_2 \frac{\Sigma_{\text{n}}^{\text{vol}}}{\sigma_y(\bar{\epsilon}^{(t-\delta t)})}\right)}{2 \frac{\Sigma_{\text{eq}}^{\text{vol}}}{\sigma_y(\bar{\epsilon}^{(t-\delta t)})}} \quad (\text{C.2})$$

451 The rate  $\delta p$  is evaluated with the help of Table 2 where  $([\dot{u}_{\text{n}}], [\dot{u}_{\text{t}}], [\dot{u}_{\text{s}}])$  are replaced by  $(h \delta \epsilon_{\text{nn}}, 2h \delta \epsilon_{\text{nt}}, 2h \delta \epsilon_{\text{ns}})$ .  
 452 Then:

$$(\delta \epsilon)_{\text{eq}} = \frac{2}{3} \sqrt{(\delta \epsilon_{\text{nn}} - \delta p)^2 + 3(\delta \epsilon_{\text{nt}})^2 + 3(\delta \epsilon_{\text{ns}})^2} \quad \text{and} \quad \eta_{\delta \epsilon} = \frac{\delta \epsilon_{\text{nn}} + 2\delta p}{3(\delta \epsilon)_{\text{eq}}} \quad (\text{C.3})$$

$$\bar{\Sigma}_{\text{nn}} = \frac{1}{q_2} H(\eta_{\delta \epsilon}, q_1 f^*(f^{(t-\delta t)})) + \frac{4}{9} D(\eta_{\delta \epsilon}, q_1 f^*(f^{(t-\delta t)})) \frac{\delta \epsilon_{\text{nn}} - \delta p}{(\delta \epsilon)_{\text{eq}}} \quad (\text{C.4})$$

$$\bar{\Sigma}_{\text{tt}} = \bar{\Sigma}_{\text{ss}} = \frac{1}{q_2} H(\eta_{\delta \epsilon}, q_1 f^*(f^{(t-\delta t)})) - \frac{2}{9} D(\eta_{\delta \epsilon}, q_1 f^*(f^{(t-\delta t)})) \frac{\delta \epsilon_{\text{nn}} - \delta p}{(\delta \epsilon)_{\text{eq}}} \quad (\text{C.5})$$

$$\bar{\Sigma}_{\text{nt}} = \frac{2}{3} D(\eta_{\delta \epsilon}, q_1 f^*(f^{(t-\delta t)})) \frac{\delta \epsilon_{\text{nt}}}{(\delta \epsilon)_{\text{eq}}} \quad (\text{C.6})$$

$$\bar{\Sigma}_{\text{ns}} = \frac{2}{3} D(\eta_{\delta \epsilon}, q_1 f^*(f^{(t-\delta t)})) \frac{\delta \epsilon_{\text{ns}}}{(\delta \epsilon)_{\text{eq}}} \quad (\text{C.7})$$

457 Then the increment of average plastic strain is computed:

$$\delta \bar{\epsilon} = \frac{\bar{\Sigma}_{\text{nn}} \delta \epsilon_{\text{nn}} + 2 \bar{\Sigma}_{\text{nt}} \delta \epsilon_{\text{nt}} + 2 \bar{\Sigma}_{\text{ns}} \delta \epsilon_{\text{ns}} + \bar{\Sigma}_{\text{tt}} \delta p + \bar{\Sigma}_{\text{ss}} \delta p}{1 - f^{(t-\delta t)}} \quad (\text{C.8})$$

458 and the porosity and plastic strain are up-dated:

$$f = f^{(t-\delta t)} + (1 - f^{(t-\delta t)}) (\delta \epsilon_{\text{nn}} + 2 \delta p) + A(\bar{\epsilon}^{(t-\delta t)}) \delta \bar{\epsilon} \quad \text{and} \quad \bar{\epsilon} = \bar{\epsilon}^{(t-\delta t)} + \delta \bar{\epsilon} \quad (\text{C.9})$$

459 Then, the following conditions are imposed:

$$\text{if } f^{(t)} < f^{(t-\delta t)} \quad \text{then } f^{(t)} = f^{(t-\delta t)}, \quad \text{and} \quad \text{if } \bar{\epsilon} < \bar{\epsilon}^{(t-\delta t)} \quad \text{then } \bar{\epsilon}^{(t)} = \bar{\epsilon}^{(t-\delta t)} \quad (\text{C.10})$$

460 The second step consists in updating the value of the cohesive stress from the following equations. The strain  
 461  $p$  is evaluated from expressions reported in Table 2 where  $([\dot{u}_{\text{n}}], [\dot{u}_{\text{t}}], [\dot{u}_{\text{s}}])$  are replaced by  $(h \epsilon_{\text{nn}}, 2h \epsilon_{\text{nt}}, 2h \epsilon_{\text{ns}})$ .  
 462 Then:

$$\epsilon_{\text{eq}} = \frac{2}{3} \sqrt{(\epsilon_{\text{nn}} - p)^2 + 3(\epsilon_{\text{nt}})^2 + 3(\epsilon_{\text{ns}})^2} \quad \text{and} \quad \eta_{\epsilon} = \frac{\epsilon_{\text{nn}} + 2p}{3 \epsilon_{\text{eq}}} \quad (\text{C.11})$$

$$\begin{cases} R_{\text{n}} = \sigma_y(\bar{\epsilon}) \left( \frac{1}{q_2} H(\eta_{\epsilon}, q_1 f^*(f)) + \frac{4}{9} D(\eta_{\epsilon}, q_1 f^*(f)) \frac{\epsilon_{\text{nn}} - p}{\epsilon_{\text{eq}}} \right) \\ R_{\text{t}} = \sigma_y(\bar{\epsilon}) \frac{2}{3} D(\eta_{\epsilon}, q_1 f^*(f)) \frac{\epsilon_{\text{nt}}}{\epsilon_{\text{eq}}} \\ R_{\text{s}} = \sigma_y(\bar{\epsilon}) \frac{2}{3} D(\eta_{\epsilon}, q_1 f^*(f)) \frac{\epsilon_{\text{ns}}}{\epsilon_{\text{eq}}} \end{cases} \quad (\text{C.12})$$

464 To the end, the cohesive stress is computed:

$$\bar{\mathbf{R}} = \begin{cases} R_{\text{n}} \frac{[u_{\text{n}}]}{[u_{\text{n}}]_{\text{max}}} \left( 1 - \exp\left(-\alpha_{\text{n}} \frac{[u_{\text{n}}]_{\text{max}}}{h}\right) \right) \\ R_{\text{t}} \frac{[u_{\text{t}}]}{[u_{\text{t}}]_{\text{max}}} \left( 1 - \exp\left(-\alpha_{\text{t}} \frac{[u_{\text{t}}]_{\text{max}}}{h}\right) \right) \\ R_{\text{s}} \frac{[u_{\text{s}}]}{[u_{\text{s}}]_{\text{max}}} \left( 1 - \exp\left(-\alpha_{\text{s}} \frac{[u_{\text{s}}]_{\text{max}}}{h}\right) \right) \end{cases} \quad (\text{C.13})$$

465 **References**

- 466 [1] C. R. Tottle, Mechanical Properties of Uranium Compounds, ANL-7070 (1965).  
 467 [2] P. Chakraborty, S. B. Biner, A unified cohesive zone approach to model the ductile to brittle transition of fracture  
 468 toughness in reactor pressure vessel steels, *Engineering Fracture Mechanics* 131 (2014) 194–209.  
 469 [3] P.-G. Vincent, Y. Monerie, P. Suquet, Porous materials with two populations of voids under internal pressure: I. Instan-  
 470 tantaneous constitutive relations, *International Journal of Solids and Structures* 46 (2009) 480–506.  
 471 [4] P.-G. Vincent, P. Suquet, Y. Monerie, H. Moulinec, Effective flow surface of porous materials with two populations of  
 472 voids under internal pressure: I. a GTN model, *International Journal of Plasticity*, 56 (2014) 45–73.  
 473 [5] A. A. Benzerga, J.-B. Leblond, Ductile Fracture by Void Growth to Coalescence, *Advances in Applied Mechanics* 44 (2010)  
 474 169–305.  
 475 [6] A. L. Gurson, Continuum Theory of Ductile Rupture by Void Nucleation and Growth: Part I—Yield Criteria and Flow  
 476 Rules for Porous Ductile Media, *Journal of Engineering Materials and Technology* 99 (1) (1977) 2–15.  
 477 [7] V. Tvergaard, Influence of voids on shear band instabilities under plane strain conditions, *International Journal of Fracture*  
 478 17 (4) (1981) 389–407.  
 479 [8] V. Tvergaard, A. Needleman, Analysis of the cup-cone fracture in a round tensile bar, *Acta Metallurgica* 32 (1) (1984)  
 480 157–169.  
 481 [9] J. Koplik, A. Needleman, Void growth and coalescence in porous plastic solids, *International Journal of Solids and*  
 482 *Structures* 24 (8) (1988) 835–853.  
 483 [10] K.-H. Schwalbe, I. Scheider, A. Cornec, Guidelines for Applying Cohesive Models to the Damage Behaviour of Engineering  
 484 Materials and Structures, Springer Science & Business Media, 2012.  
 485 [11] A. Needleman, Some issues in cohesive surface modeling, *Procedia IUTAM* 10 (2014) 221 – 246, mechanics for the World:  
 486 Proceedings of the 23rd International Congress of Theoretical and Applied Mechanics, ICTAM2012.  
 487 [12] D. Dugdale, Yielding of steel sheets containing slits, *Journal of the Mechanics and Physics of Solids* 8 (2) (1960) 100 –  
 488 104.  
 489 [13] G. I. Barenblatt, The formation of equilibrium cracks during brittle fracture. General ideas and hypotheses. Axially-  
 490 symmetric cracks, *Journal of Applied Mathematics and Mechanics* 23 (3) (1959) 622–636.  
 491 [14] A. Needleman, A Continuum Model for Void Nucleation by Inclusion Debonding, *Journal of Applied Mechanics* 54 (3)  
 492 (1987) 525–531.  
 493 [15] A. Needleman, An analysis of tensile decohesion along an interface, *Journal of the Mechanics and Physics of Solids* 38 (3)  
 494 (1990) 289–324.  
 495 [16] V. Tvergaard, J. W. Hutchinson, The relation between crack growth resistance and fracture process parameters in elastic-  
 496 plastic solids, *Journal of the Mechanics and Physics of Solids* 40 (6) (1992) 1377–1397.  
 497 [17] I. Scheider, W. Brocks, Simulation of cup-cone fracture using the cohesive model, *Engineering Fracture Mechanics* 70 (14)  
 498 (2003) 1943–1961.  
 499 [18] J.-L. Chaboche, F. Feyel, Y. Monerie, Interface debonding model: a viscous regularization with a limited rate dependency,  
 500 *International Journal of Solids and Structures* 38 (18) (2001) 3127–3160.  
 501 [19] T. Siegmund, A. Needleman, A numerical study of dynamic crack growth in elastic-viscoplastic solids, *International*  
 502 *Journal of Solids and Structures* 34 (7) (1997) 769–787.  
 503 [20] K. L. Nielsen, J. W. Hutchinson, Cohesive traction-separation laws for tearing of ductile metal plates, *International Journal*  
 504 *of Impact Engineering* 48 (2012) 15–23.  
 505 [21] P. B. Woelke, M. D. Shields, J. W. Hutchinson, Cohesive zone modeling and calibration for mode I tearing of large ductile  
 506 plates, *Engineering Fracture Mechanics* 147 (2015) 293–305.  
 507 [22] R. G. Andersen, P. B. Woelke, K. L. Nielsen, Cohesive traction-separation relations for plate tearing under mixed mode  
 508 loading, *European Journal of Mechanics / A Solids* 71 (2018) 199–209.  
 509 [23] R. G. Andersen, C. L. Felter, K. L. Nielsen, Micro-mechanics based cohesive zone modeling of full scale ductile plate  
 510 tearing: From initiation to steady-state, *International Journal of Solids and Structures* 160 (2019) 265–275.  
 511 [24] Y. Bao, T. Wierzbicki, On fracture locus in the equivalent strain and stress triaxiality space, *International Journal of*  
 512 *Mechanical Sciences* 46 (1) (2004) 81–98.  
 513 [25] A. A. Benzerga, J.-B. Leblond, A. Needleman, V. Tvergaard, Ductile failure modeling, *International Journal of Fracture*  
 514 201 (1) (2016) 29–80.  
 515 [26] V. Tvergaard, J. W. Hutchinson, Effect of strain-dependent cohesive zone model on predictions of crack growth resistance,  
 516 *International Journal of Solids and Structures* 33 (20) (1996) 3297–3308.  
 517 [27] V. Tvergaard, Relations between Crack Growth Resistance and Fracture Process Parameters Under Large Scale Yielding,  
 518 in: *IUTAM Symposium on Nonlinear Analysis of Fracture, Solid Mechanics and its Applications*, Springer, Dordrecht,  
 519 1997, pp. 93–104.  
 520 [28] A. Banerjee, R. Manivasagam, Triaxiality dependent cohesive zone model, *Engineering Fracture Mechanics* 76 (12) (2009)  
 521 1761–1770.  
 522 [29] M. Rajendran, I. Scheider, A. Banerjee, Stress State Dependent Cohesive Zone Model for Thin Walled Structures, *Key*  
 523 *Engineering Materials* 417-418 (2010) 353–356.  
 524 [30] I. Scheider, Derivation of separation laws for cohesive models in the course of ductile fracture, *Engineering Fracture*  
 525 *Mechanics* 76 (10) (2009) 1450–1459.  
 526 [31] T. Siegmund, W. Brocks, Prediction of the Work of Separation and Implications to Modeling, *International Journal of*  
 527 *Fracture* 99 (1-2) (1999) 97–116.

- 528 [32] T. Siegmund, W. Brocks, A numerical study on the correlation between the work of separation and the dissipation rate  
529 in ductile fracture, *Engineering Fracture Mechanics* 67 (2) (2000) 139–154.
- 530 [33] M. Anvari, I. Scheider, C. Thaulow, Simulation of dynamic ductile crack growth using strain-rate and triaxiality-dependent  
531 cohesive elements, *Engineering Fracture Mechanics* 73 (15) (2006) 2210–2228.
- 532 [34] M. Anvari, J. Liu, C. Thaulow, Dynamic ductile fracture in aluminum round bars: experiments and simulations, *International  
533 Journal of Fracture* 143 (4) (2007) 317–332.
- 534 [35] M. Găărăjeu, P. Suquet, Effective properties of porous ideally plastic or viscoplastic materials containing rigid particles,  
535 *Journal of the Mechanics and Physics of Solids* 45 (6) (1997) 873–902.
- 536 [36] C. C. Chu, A. Needleman, Void Nucleation Effects in Biaxially Stretched Sheets, *Journal of Engineering Materials and  
537 Technology* 102 (3) (1980) 249–256.
- 538 [37] J.-C. Michel, P. Suquet, F. Thébaud, Une modélisation du rôle des interfaces dans le comportement des composites à  
539 matrice métallique, *Revue Européenne des Éléments Finis* 3 (4) (1994) 573–595.
- 540 [38] Y. Monerie, V. Acary, Formulation dynamique d’un modèle de zone cohésive tridimensionnel couplant endommagement  
541 et frottement, *Revue Européenne des Éléments Finis* 10 (02-03-04) (2001) 489–503.
- 542 [39] P. M. Suquet, Discontinuities and Plasticity, in: *Nonsmooth Mechanics and Applications*, International Centre for Me-  
543 chanical Sciences, Springer, Vienna (1988) 279–340.
- 544 [40] J. Oliver, M. Cervera, O. Manzoli, Strong discontinuities and continuum plasticity models: the strong discontinuity  
545 approach, *International Journal of Plasticity* 15 (3) (1999) 319–351.
- 546 [41] F. M. Rashid, A. Banerjee, Implementation and validation of a triaxiality dependent cohesive model: experiments and  
547 simulations, *International Journal of Fracture* 181 (2) (2013) 227–239.
- 548 [42] F.M. Rashid, A. Banerjee, Simulation of fracture in a low ductility aluminum alloy using a triaxiality dependent cohesive  
549 model, *Engineering Fracture Mechanics* 179 (C) (2017) 1–12.
- 550 [43] J. J. C. Remmers, R. de Borst, C. V. Verhoosel, A. Needleman, The cohesive band model: a cohesive surface formulation  
551 with stress triaxiality, *International Journal of Fracture* 181 (2) (2013) 177–188.
- 552 [44] N. Aravas, On the Numerical Integration of a Class of Pressure-Dependent Plasticity Models, *International Journal for  
553 Numerical Methods in Engineering* 24 (1987) 1395–1416.
- 554 [45] M. Jean, V. Acary, Y. Monerie, Non-smooth contact dynamics approach of cohesive materials, *Philosophical Transactions  
555 of the Royal Society A: Mathematical, Physical and Engineering Sciences* 359 (1789) (2001) 2497–2518.
- 556 [46] J. C. Michel, H. Moulinec, P. Suquet, Effective properties of composite materials with periodic microstructure: a compu-  
557 tational approach, *Computer Methods in Applied Mechanics and Engineering* 172 (1) (1999) 109–143.
- 558 [47] F. Perales, S. Bourgeois, A. Chrysochoos, Y. Monerie, Two field multibody method for periodic homogenization in  
559 fracture mechanics of nonlinear heterogeneous materials, *Engineering Fracture Mechanics* 75 (11) (2008) 3378 – 3398,  
560 local Approach to Fracture (1986–2006): Selected papers from the 9th European Mechanics of Materials Conference.
- 561 [48] F. Perales, F. Dubois, Y. Monerie, B. Piar, L. Stainier, A NonSmooth Contact Dynamics-based multi-domain solver,  
562 *European Journal of Computational Mechanics* 19 (4) (2010) 389–417.
- 563 [49] V. Acary, Y. Monerie, Nonsmooth fracture dynamics using a cohesive zone approach, *Research Report*, INRIA (2006).
- 564 [50] M. Jean, The non-smooth contact dynamics method, *Computer Methods in Applied Mechanics and Engineering* 177 (3)  
565 (1999) 235–257.
- 566 [51] M. Ortiz, A. Pandolfi, Finite-deformation irreversible cohesive elements for three-dimensional crack-propagation analysis,  
567 *International Journal for Numerical Methods in Engineering* 44 (9) (1999) 1267–1282.
- 568 [52] W. Brocks, A. Eberle, S. Fricke, H. Veith, Large stable crack growth in fracture mechanics specimens, *Nuclear Engineering  
569 and Design* 151 (2) (1994) 387–400.
- 570 [53] T. Siegmund, W. Brocks, The Role of Cohesive Strength and Separation Energy for Modeling of Ductile Fracture, in  
571 *Fatigue and Fracture Mechanics: 30th Volume*, ed. K. Jerina and P. Paris, West Conshohocken, PA: ASTM International  
572 (2000), 139–151.
- 573 [54] F. Perales, Fissuration des matériaux à gradient de propriétés : application au Zircaloy hydruré, Ph.D. thesis, Montpellier  
574 2 (2005).
- 575 [55] W. Brocks, D. Klingbeil, G. Künecke, D.-Z. Sun, Application of the Gurson Model to Ductile Tearing Resistance, in  
576 *Constraint Effects in Fracture Theory and Applications: Second Volume*, ed. M. Kirk and A. Bakker, West Conshohocken,  
577 PA: ASTM International (1995), 232–252.
- 578 [56] ASTM, ASTM e1820-18, standard test method for measurement of fracture toughness, Standard, ASTM International,  
579 West Conshohocken, PA (Jan. 2018).
- 580 [57] X.-K. Zhu, J. A. Joyce, Review of fracture toughness (G, K, J, CTOD, CTOA) testing and standardization, *Engineering  
581 Fracture Mechanics* 85 (2012) 1–46.
- 582 [58] J. Besson, Continuum models of ductile fracture: A review, *International Journal of Damage Mechanics* 19 (2010) 3–52.
- 583 [59] N. Blal, L. Daridon, Y. Monerie, S. Pagano, Artificial compliance inherent to the intrinsic cohesive zone models: Criteria  
584 and application to planar meshes, *International Journal of Fracture* 178 (1-2) (2012) 71–83.
- 585 [60] V. Tomar, J. Zhai, M. Zhou, Bounds for element size in a variable stiffness cohesive finite element model, *International  
586 Journal for Numerical Methods in Engineering* 61 (11) (2004) 1894–1920.
- 587 [61] H. D. Espinosa, P. D. Zavattieri, A grain level model for the study of failure initiation and evolution in polycrystalline  
588 brittle materials. Part I: Theory and numerical implementation, *Mechanics of Materials* 35 (3) (2003) 333–364.